Falling film on an anisotropic porous medium

Sanghasri Mukhopadhyay, Nicolas Cellier, Christian Ruyer-Quil

Falling film on an anisotropic porous medium

Sanghasri Mukhopadhyay[*1], Nicolas Cellier [†2]& Christian ruyer-Quil[‡3]

[1, 2, 3]Université Savoie Mont Blanc, CNRS, LOCIE, 73000 Chambéry, France

Abstract

The stability and dynamics of a falling liquid film over a porous medium are studied using a one-domain approach, extending the work by [1] to account for the anisotropy of the porous medium. In the isotropic case, our stability analysis shows a significant departure from the effective no-slip boundary condition (no-slip model) that was proposed by [1]. We conjecture that the origin of this discrepancy is a significant exchange of mass at the liquid-porous interface. Anisotropy does not affect the threshold of linear instability. However, a non-trivial dual effect of anisotropy on the film stability is observed depending on the permeability of the porous medium. Three-equation models have been derived within the lubrication theory in terms of the exact mass balance and averaged momentum balances in the porous and liquid layers. In the nonlinear regime, the intensity of the exchange of mass at the liquid-porous interface is significant and impact the amplitude of the capillary waves, which precede the one-humped solitary waves. Anisotropy has a dual effect by damping capillary waves at large permeabilities and enhancing them at low permeabilities.

Keywords— thin films, low-dimensional models, porous medium

1 Introduction

Falling liquid film flows are commonly used in chemical engineering whenever pressure drops or boiling may be avoided. Classic examples are evaporators in the food industry for the concentration of heat-sensitive products [2] or distillation columns for the separation of components with close boiling points, in which case large-scale separation towers are required. For the latter, the configuration of choice is a countercurrent contact between an upward gas and a downward liquid film distributed on a structured packing. The ideal design of structured packing shall limit the pressure drops and improve the mass transfer efficiency. The metal sheets constituting the packing are generally perforated to promote the distribution of the liquid and further reduce the pressure drop. For similar reasons, new wire gauze packing has been proposed [3].

Instabilities of the liquid film are known to significantly enhance heat or mass transfer by promoting surface waves [4, 5] and this mechanism is generally believed to play a crucial role in the efficiency of packed bed exchangers. However, little is known about the permeability of the wire gauze or perforated sheets on the liquid film instabilities. In an attempt to better understand this effect on the film surface-wave hydrodynamics, we consider in this study a falling liquid film flow on an anisotropic porous medium. The introduction of different stream-wise and cross-stream permeabilities of an otherwise homogeneous porous medium is a simplified modelling of the orientation of the perforations of metal sheets and wire orientations of gauze packings.

The onset of surface-wave instabilities in film flows on an inclined impermeable plate is well documented (see, for instance, the reviews by [6–8]). However, the hydrodynamics of a liquid film flow over a porous substrate has attracted far less attention. [9] was the first to consider a stability problem of a thin fluid layer

---

[*]msanghasri@gmail.com

[†]contact@nicolas-cellier.net

[‡]Christian.Ruyer-Quil@univ-smb.fr

flowing down an inclined permeable wall, proceeding with the same formulation as [10] had done for falling film over an impermeable wall. [9] used the Darcy law to describe the flow in porous medium and Beavers-Joseph slip boundary conditions at the fluid-porous interface. Pascal showed that in the case of a low superficial velocity in the porous medium, the presence of the porous medium could be modelled by an impermeable wall with a Navier slip boundary condition. Pascal observed a destabilising effect of the Navier slip condition on the instability threshold. This finding was confirmed by the nonlinear analysis of [11]. This problem was revisited by [12] within the framework of the weighted-residual approach proposed initially by [13]. A non-trivial stabilisation of the film flow by the Navier slip condition was reported far from the instability threshold. However, this surprising result can be explained by a choice of scaling that was different from the one used by [9] and [11]. [14] have introduced a two-sided approach by resolving the Darcy-Brinkman equation in the porous medium and by modelling the porous-fluid interface with a stress jump boundary conditions [15]. This approach introduces a jump coefficient, whose expression depends on the detail of the spatial variations of the porous structure near the interface.

One alternative modelling approach proposed by [16] has been employed by many authors, for instance by [17] to study heat transfer, and by [1] to consider the stability and dynamics of a falling film over a porous medium, or by [18] to study transport phenomena etc. In this approach, the total system of the fluid and porous medium is considered as a single composite domain, and the characteristic properties like porosity and permeability are taken to be continuous throughout the domain. In the transition of the liquid and porous layer, a thin heterogeneous transition layer exists in which permeability and porosity present a rapid dramatic but continuous change. The main advantage of this approach, referred to as the one-domain approach, in contrast to the two-domain approach presented above, is the elimination of interfacial boundary conditions. [19] had numerically solved the linear stability eigenvalue problem of the two-sided coupled fluid porous model using the Chebyshev collocation method. They have considered the Darcy law as a porous medium momentum transport model and Beavers-Joseph slip boundary condition at the interface. They reported three modes of instability: surface mode, shear mode, and a new one called porous mode associated with the flow in a porous medium. They also claimed that qualitatively, one and two-sided model gives similar results for moderately low permeability and substrate thickness.

Until here, all the above-discussed studies have been done considering the porous medium as isotropic and homogeneous. Convection in an anisotropic porous medium was first considered by [20] and [21]. Later, various researcher have explored the anisotropy and inhomogeneity effect of porous medium in the context of heat transfer [22–24]. [25] were the first to work on hydrodynamic stability of falling film over an anisotropic and inhomogeneous porous medium. They considered a generalised Darcy law to describe the flow in the porous medium coupled to the Beavers and Joseph boundary condition at the interface. They discussed the surface instability mode as well as the shear mode of linear instability and concluded that anisotropy has no visible effect on the linear stability of the surface mode. Later, [26] provided a detailed analytical description of the flow over an anisotropic and inhomogeneous porous medium. They solved the linear eigenvalue problem constructed under the long-wave assumption up to first-order in the wavenumber and concluded that the anisotropy effect arises only at higher order. In the recent past, [27] have performed a temporal linear stability analysis, under the Orr Sommerfeld framework, of a pressure-driven laminar fully developed flow in a horizontal channel bounded by an anisotropic and inhomogeneous porous wall at the bottom and a rigid wall at the top. They considered two immiscible fluids of stratified density and viscosity. They employed the Darcy model for flow in a porous medium with Beavers and Joseph boundary conditions at the porous-liquid interface. They revealed that increasing anisotropy (relative increase of permeability in the flow direction) stabilises the porous and the interface mode.

In this paper, we consider the effect of an anisotropic permeability on the hydrodynamics of falling films flowing down a porous medium on a saturated porous substrate sealed at its bottom by an impermeable condition. Section §2 presents the governing equations for the one-domain and two-domain approaches. Section §3 is devoted to the linear stability of the Nusselt uniform-film solution and compares the one-domain and two-domain stability analysis. An extension of the weighted-residual strategy followed by [1] is detailed in section §4. Nonlinear travelling wave solutions and time-dependent simulations are discussed in sections §5
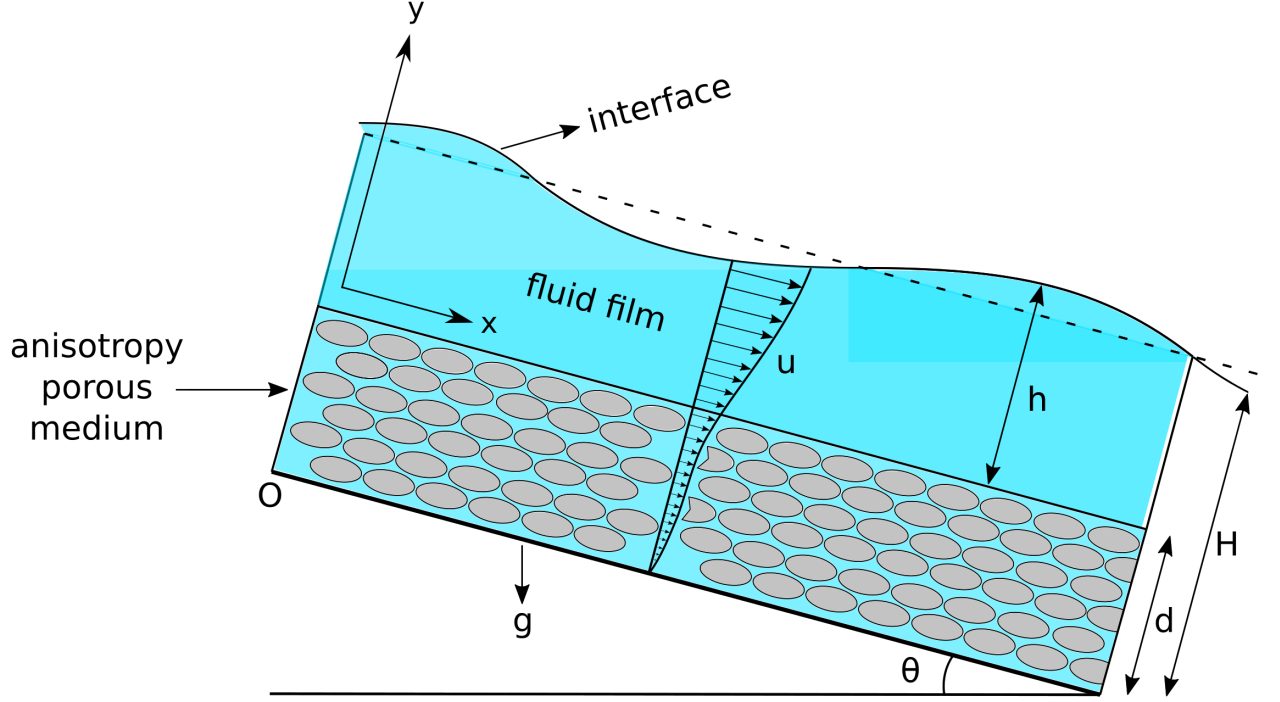
Figure 1: Schematic diagram of a falling film over an anisotropic saturated porous medium.

and §6. Section §7 concludes the present study.

2 Governing equation

We consider a two dimensional viscous, incompressible thin liquid film flowing under the action of gravity on a saturated inclined anisotropic porous plate of height d. The porous medium is considered to be bounded on one side by a rigid wall. (see figure 1). Fundamental fluid properties, i.e. density (ρ), surface tension (σ), kinematic viscosity (ν) are supposed to remain constant. The thickness of the entire domain, comprising the porous substrate and the liquid layer, is denoted by H. The origin of the vertical axis is chosen at the solid boundary, x refers to the coordinate in the flow direction and y to the cross-stream direction. The porous medium is uniform, with a constant porosity ε, but anisotropic, with different permeabilities κ_{1H} and κ_{2H} in the streamwise x and cross-stream y directions. Two different approaches are available to describe such flows. The first one, nicknamed the 'one-domain' approach, considers a composite domain where the properties of the medium vary continuously from those of the porous medium to those of the liquid medium in a thin transitional region which replaces the liquid-porous interface. The second approach is more straightforward. The liquid and porous medium are connected by a liquid-porous interface for which adequate boundary conditions are formulated. These two approaches will be contrasted in the following study.

2.1 One-domain approach

We introduce a heterogeneous transition layer where material properties of the porous medium, such as porosity (ε) and permeability in the y-direction (κ_y) show significant and continuous variations from constant values ε_H and κ_{2H} in porous medium to the values 1 and ∞ in the liquid layer. Apart from this zone, the porous medium is considered to be homogeneous.

3

The governing equations are given by [28]:

$$u_x + v_y = 0, \tag{1a}$$

$$\frac{\rho}{\varepsilon}\left[u_t + \frac{1}{\varepsilon}(uu_x + vu_y) + uv\frac{\partial}{\partial y}\left(\frac{1}{\varepsilon}\right)\right] = -p_x + \frac{\mu}{\varepsilon}(u_{xx} + u_{yy}) - \frac{\mu u}{\kappa_x(y)} + \rho g\sin\theta, \tag{1b}$$

$$\frac{\rho}{\varepsilon}\left[v_t + \frac{1}{\varepsilon}(uv_x + vv_y) + \frac{v^2}{\varepsilon}\frac{\partial}{\partial y}\left(\frac{1}{\varepsilon}\right)\right] = -p_y + \frac{\mu}{\varepsilon}(v_{xx} + v_{yy}) - \frac{\mu v}{\kappa_y(y)} - \rho g\cos\theta, \tag{1c}$$

where indices refer to time and space derivatives (with the exception of the permeabilities κ_x and κ_y). As we have combined the governing equations for the liquid and the porous layer together, the boundary conditions at the porous liquid interface are satisfied automatically. It is sufficient to choose the boundary conditions at the lower boundary ($y = 0$) and at the free surface ($y = H$). The bottom of the substrate $y = 0$ is an impermeable wall

$$u = 0, \quad v = 0 \quad \text{at} \quad y = 0. \tag{1d}$$

At the free surface $y = H$, a passive atmosphere with a constant pressure is assumed. Thus the kinematic condition and the continuity of the stresses write

$$H_t + uH_x = v, \tag{1e}$$

$$\frac{1}{1 + H_x^2}\left[2\mu H_x^2(v_y - u_x) + \mu(u_y + v_x)(1 - H_x^2)\right] = 0, \tag{1f}$$

$$p(1 + H_x^2) - 2\mu(H_x^2 u_x - (u_y + v_x)H_x + v_y) = \frac{\sigma H_{xx}}{(1 + H_x^2)^{1/2}}. \tag{1g}$$

The properties of the porous medium, porosity $\varepsilon(y)$ and permeabilities $\kappa_x(y)$, $\kappa_y(y)$ vary continuously through the domain

$$\varepsilon(y) = \frac{1 + \varepsilon_H}{2} + \frac{1 - \varepsilon_H}{2}\tanh[(y - \delta)/\Delta], \tag{1h}$$

$$\frac{1}{\kappa_x(y)} = \frac{1}{\kappa_{1H}}\left[\frac{1}{2} - \frac{1}{2}\tanh\frac{(y - d)}{\Delta}\right], \tag{1i}$$

$$\frac{1}{\kappa_y(y)} = \frac{1}{\kappa_{2H}}\left[\frac{1}{2} - \frac{1}{2}\tanh\frac{(y - d)}{\Delta}\right]. \tag{1j}$$

Where κ_{1H} and κ_{2H} are the constant values of $\kappa_x(y)$ and $\kappa_y(y)$ respectively inside the porous medium in the stream-wise and cross-stream directions. The distribution of $\varepsilon(y)$, $\kappa_x(y)$ and $\kappa_y(y)$ are assumed to follow a tangent hyperbolic profile which allows to control easily the thickness of the transition layer of typical thickness Δ. In the limit $\varepsilon \to 1$, $\kappa_x, \kappa_y \to \infty$ the equations (1b) and (1c) lead back to the classical momentum balance for flow of an incompressible fluid on a rigid wall. System (1) is an extension of the problem formulated by [1] where an isotropic porous layer has been considered.

The following dimensionless quantities, denoted by a tilde, are defined with the choice of characteristic scales for velocity, length and pressure as U_N, H_N and $\rho g H_N$ respectively, where H_N is the thickness of the entire porous and liquid layer, U_N stands for free-surface velocity of the uniform film which characterises the wavy motion of the free surface.

$$\tilde{u} = \frac{u}{U_N}; \quad \tilde{v} = \frac{v}{U_N}; \quad \tilde{x} = \frac{x}{H_N}; \quad \tilde{y} = \frac{y}{H_N}; \quad \tilde{t} = \frac{t}{H_N}U_N; \quad \tilde{H} = \frac{H}{H_N};$$

$$\tilde{p} = \frac{p}{\rho U_N^2}; \quad \tilde{\kappa}_x(y) = \frac{\kappa_x(y)}{H_N^2}, \quad \tilde{\kappa}_y(y) = \frac{\kappa_y(y)}{H_N^2} \quad \delta = \frac{d}{H_N}, \quad \tilde{\Delta} = \frac{\Delta}{H_N}. \tag{2}$$

Where $H = h + d$ is the extension of the entire layer, h is the thickness of the liquid layer and d is porous layer thickness.

The dimensionless governing equations for the liquid and porous medium follow (for convenience we omit the tilde).

$$u_x + v_y = 0, \tag{3a}$$

$$\frac{Re}{\varepsilon(y)} \left[u_t + \frac{1}{\varepsilon}(uu_x + vu_y) + uv\frac{\partial}{\partial y}\left(\frac{1}{\varepsilon}\right) \right] = -Re\,p_x + \frac{1}{\varepsilon}(u_{xx} + u_{yy}) - \frac{u}{k_x(y)}$$
$$+ \frac{Re}{Fr^2}, \tag{3b}$$

$$\frac{Re}{\varepsilon(y)} \left[v_t + \frac{1}{\varepsilon}(uv_x + vv_y) + v^2\frac{\partial}{\partial y}\left(\frac{1}{\varepsilon}\right) \right] = -Re\,p_y + \frac{1}{\varepsilon}(v_{xx} + v_{yy}) - \frac{v}{k_y(y)}$$
$$- \cot\theta\frac{Re}{Fr^2}. \tag{3c}$$

The boundary conditions are:

$$\text{at} \quad y = 0, \qquad u = 0, \quad v = 0. \tag{3d}$$

The free surface $y = H$ we have the conditions:

$$H_t + uH_x = v, \tag{3e}$$

$$-4u_xH_x + (u_y + v_x)(1 - H_x^2) = 0, \tag{3f}$$

$$p - \frac{2}{Re(1 + H_x^2)}(H_x^2 u_x - (u_y + v_x)H_x + v_y) = -\frac{WeH_{xx}}{(1 + H_x^2)^{3/2}}. \tag{3g}$$

The dimensionless expression for the porosity and permeability are:

$$\varepsilon(y) = \frac{1 + \varepsilon_H}{2} + \frac{1 - \varepsilon_H}{2}\tanh[(y - \delta)/\Delta], \tag{3h}$$

$$\frac{1}{\kappa_x(y)} = \frac{1}{Da}\left(\frac{1}{2} - \frac{1}{2}\tanh[(y - \delta)/\Delta]\right), \tag{3i}$$

$$\frac{1}{\kappa_y(y)} = \frac{\xi}{Da}\left(\frac{1}{2} - \frac{1}{2}\tanh[(y - \delta)/\Delta]\right). \tag{3j}$$

System (3) involves five dimensionless parameters. Besides the Reynolds, Froude, Weber and Darcy numbers Re, Fr, We and Da

$$Re = \frac{H_N U_N}{\nu}, \quad Fr = \frac{U_N}{\sqrt{g\sin\theta H_N}}, \quad We = \frac{\sigma}{\rho H_N U_N^2}, \quad Da = \frac{\kappa_{1H}}{H_N^2}. \tag{4}$$

We define an anisotropy parameter ξ as

$$\xi = \kappa_{1H}/\kappa_{2H}, \tag{5}$$

which compares the permeabilities in the bulk of the porous medium. It is useful to introduce the Kapitza number $Ka = \sigma/[\rho\nu^{4/3}(g\sin\theta)^{1/3}] = WeFr^{4/3}Re^{2/3}$ which compares surface tension, viscosity and gravity. This parameter depends only on the fluid properties and the inclination of the wall.

2.2 Two-domain approach

In the two-domain approach, the porous and liquid layers form separate layers with an interface, where the material properties of the porous medium (e.g. porosity, permeability etc.) are discontinuous. Here we use the formulation introduced by [14] and extend their work to the case of an anisotropic porous medium. We denote by (u, v, p) and (u_p, v_p, p_p) the variables in the liquid and porous domains respectively. The governing equations consist of the Navier-Stokes equations for an incompressible flow in the liquid layer

$$\partial_x u + \partial_y v = 0, \tag{6a}$$

$$Re\left[\partial_t u + u\partial_x u + v\partial_y u\right] = -Re\partial_x p + (\partial_{xx}u + \partial_{yy}u) + \frac{Re}{Fr^2}, \tag{6b}$$

$$Re\left[\partial_t v + u\partial_x v + v\partial_y v\right] = -Re\partial_y p + (\partial_{xx}v + \partial_{yy}v) - \cot\theta\frac{Re}{Fr^2}, \tag{6c}$$

and, in the porous layer

$$\partial_x u_p + \partial_y v_p = 0, \tag{6d}$$

$$\frac{Re}{\varepsilon_H}\partial_t u_p = -Re\partial_x p_p + \frac{1}{\varepsilon_H}\left(\partial_{xx}u_p + \partial_{yy}u_p\right) - \frac{u_p}{Da} + \frac{Re}{Fr^2}, \tag{6e}$$

$$\frac{Re}{\varepsilon_H}\partial_t v_p = -Re\partial_y p_p + \frac{1}{\varepsilon_H}\left(\partial_{xx}v_p + \partial_{yy}v_p\right) - \frac{\xi}{Da}v_p - \cot\theta\frac{Re}{Fr^2}, \tag{6f}$$

where the superficial velocity u_p in the porous layer is assumed to remain small as compared to the fluid velocity u so that advection terms have been dropped out in (6e) and (6f). These terms are negligible in comparison to viscous drag and Brinkman diffusion terms in the porous medium. (6) is completed by the no-slip and no penetration condition at the wall

$$\text{at} \quad y = 0, \qquad u_p = 0, \quad v_p = 0. \tag{6g}$$

At the interface of the porous and the liquid $y = \delta$, we use the model initially proposed by [15] and later used by [14]. Whereas the velocity field is assumed to remain continuous at the interface, a jump of the tangential shear stress is introduced, which gives

$$u = u_p, \qquad v = v_p, \tag{6h}$$

$$\frac{1}{\varepsilon_H}\partial_y u_p - \partial_y u = \frac{\beta}{\sqrt{Da}}u_p, \tag{6i}$$

$$-p_p + \frac{2}{\varepsilon_H}\partial_y v_p = -p + 2\partial_y v, \tag{6j}$$

where β is the dimensionless jump coefficient. At the free-surface $y = H$, the kinematic condition (3e), and the continuity of stresses (3f), (3g) hold. A limitation of the two-domain approach is that the jump coefficient β is a priori unknown and dependent on the permeability of the porous medium. [29] provided an explicit formulation of β as a function of the details of the spatial variations of the porous structure near the interface. However, we will see in the next section that the computation of the base flow offers a convenient way to tabulate this parameter.

2.3 Base flow

The base flow corresponds to a film of constant thickness whose stability characteristics are investigated within the framework of linear stability analysis. Let (U_B, P_B) represents the solution for the base flow, then it satisfies:

$$\frac{u_{yy}}{\varepsilon(y)} - \frac{u}{\kappa_x(y)} + \frac{Re}{Fr^2} = 0, \tag{7a}$$

$$-Re p_y - \frac{\cot\theta Re}{Fr^2} = 0. \tag{7b}$$
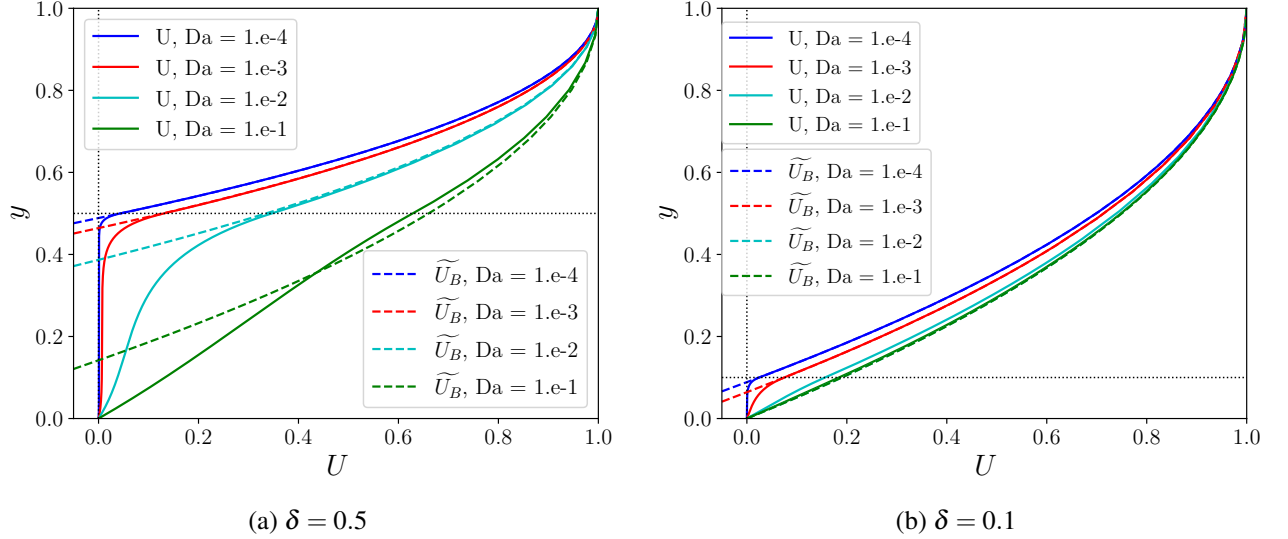
(a) $\delta = 0.5$ (b) $\delta = 0.1$

Figure 2: Base-flow velocity profile $U_B(y)$ and approximated base-flow velocity profile $\tilde{U}(y)$ as a function of the cross-stream coordinate y for different permeabilities, when $\varepsilon_H = 0.78$, $\Delta = 0.001$, (a) $\delta = 0.5$, and (b) $\delta = 0.1$.

With the boundary conditions:

$$u = 0, \quad \text{at} \quad y = 0, \tag{7c}$$

$$u_y = 0, \quad \text{at} \quad y = H, \tag{7d}$$

$$p = 0 \quad \text{at} \quad y = H. \tag{7e}$$

Following [1], we introduce, for our convenience, a linear differential operator L, as $L \equiv \partial_{yy} - (\varepsilon/\kappa_x) Id$ to account for the viscous drag and viscous diffusion at the solid phase in the porous medium, where Id refers to the identity operator. By construction, $U_B(y = H) = 1$ as the free surface velocity of the uniform film solution is the velocity scale. Therefore (7a) can be written as

$$Lu = -\frac{Re}{Fr^2}\varepsilon, \quad u(0) = u'(0) = 0, \quad u(H) = 1, \tag{8}$$

which is a boundary-value problem with an adjustable parameter Re/Fr^2, which depends on the base flow solution U_B, and therefore is a function of the domain geometry (H, δ) and the Darcy number Da. The anisotropy of the porous medium does not affect the base flow, which is unidirectional.

We use AUTO07p software [30] to solve numerically (8) by continuation. To start the continuation, we have considered the free surface flow on a rigid wall. ($\varepsilon = 1$, $\kappa_x^{-1} = 0$). We then gradually adjust the porosity and permeability to the desired values. AUTO07p is allowed to adapt the mesh as it is equipped with a mesh refinement algorithm, so it can easily compute the changes of porosity and permeability at the liquid porous interface. We have checked for the presence of a sufficient number of mesh points in the transition layer. We have also checked that the thickness of the transitional layer Δ is sufficiently low to ensure that the solution is independent of this parameter.

Figure 2a compares the base-flow solution for different values of the Darcy number. For all the numerical results presented in this work, the porous region is chosen relatively thick with δ set to 0.5. As stated above, the transitional layer is thin enough with $\Delta = 0.001$ (this value is kept constant in the remainder of this work). Even at a low value of the Darcy number ($Da = 0.001$), a significant flow is observable at the top of the porous layer, even though the velocity profile in the bulk of the porous medium is flat and nearly negligible. Three regions can be considered, two momentum boundary layers (Brinkman layers) at the top and bottom of the porous medium, for which a significant shear is observed, and a Darcy region in between where the velocity

Da	10^{-1}	10^{-2}	10^{-3}	10^{-4}
β	0.21	0.20	0.16	0.01

Table 1: Numerical computations of the jump coefficient β for different values of Darcy number Da, when $\varepsilon_H = 0.78$ $\delta = 0.5$ and $\Delta = 0.001$.

is nearly uniform. For the higher value $Da = 0.01$, the shear exerted by the liquid flow affects the flow in the porous medium in its entirety and the Darcy region is removed. The extension of the Brinkman layers can be determined by balancing the viscous diffusion $\partial_{yy}u/\varepsilon_H$ and the Darcy drag u/Da, which gives the estimate $\delta_B = \sqrt{Da/\varepsilon_H}$.

[1] have argued that, when the Brinkman layers do not invade the whole porous medium, i.e. $\delta_B < \delta/2$, an approximate solution to the base flow is a liquid film on a solid substrate for which the no-slip condition is displaced at $y = 1 - \delta + \delta_B$, which gives the approximate solution $\tilde{U}_B$

$$\tilde{U}_B = \frac{(\delta - \delta_B - y)(y - 2H + \delta - \delta_B)}{(H - \delta + \delta_B)^2}, \tag{9}$$

and therefore

$$\frac{Re}{Fr^2} = -\frac{d^2\tilde{U}_B}{dy^2} \approx \frac{2}{(H - \delta + \delta_B)^2}. \tag{10}$$

The base-flow velocity, U_B solution to (8), is compared to its approximation $\tilde{U}_B$, solution to (9), in figure 2a. An excellent agreement in the liquid region of the flow is observed. Since the instability of the film is a free-surface instability, [1] thus concluded that the instability of a film on a porous substrate could be reduced to the instability of a film on an effective impermeable boundary located at the bottom $y = \delta - \delta_B$ of the top Brinkman layer. In the next section, we will reconsider the effect of the anisotropy of the porous substrate on the linear stability of the film.

The base-flow solution U_B of the one-domain formulation offers a convenient way to adjust the jump coefficient β of the two-domain formulation. Following [1], we used the stress continuity condition (6i) to compute β from the base flow profile U_B, where $\partial_y u|_\delta \approx U'_B(\delta + 3\Delta)$, $\partial_y u_p|_\delta \approx U'_B(\delta - 3\Delta)$ and $u_p \approx U_B(\delta)$. Table 1 presents the result of our computation. β increases with the Darcy number as a less permeable porous presents a more pronounced jump of stresses at its boundary. The jump coefficient β being known, we next compute the two-domain base-flow solution and compare it on figure 3 to the base-flow solution for the one-domain approach. The comparison shows that the two approaches yield very close results.

3 Linear stability analysis

We consider a uniform layer of unit thickness $H = 1$ and introduce a perturbation expansion of the base flow solution:

$$\begin{aligned}
u(x,y,t) &= U_B(y) + ub(x,y,t), \\
v(x,y,t) &= vb(x,y,t), \\
p(x,y,t) &= P_B(x) + pb(x,y,t).
\end{aligned} \tag{11}$$

We further introduce a stream function for the perturbation quantities and a modal decomposition with wavenumber $k = k_r + ik_i$ and phase speed $c = c_r + ic_i$,

$$\Psi(x,y,t) = \psi(y)\exp[ik(x - ct)], \tag{12}$$

so that $ub = \dfrac{\partial \Psi}{\partial y}$ and $vb = -\dfrac{\partial \Psi}{\partial x}$ automatically satisfy continuity equation for the perturbed flow.
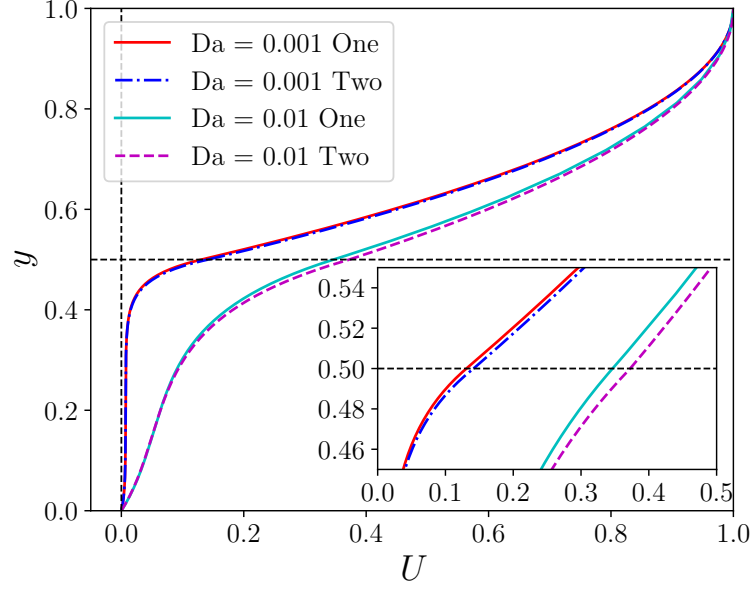
Figure 3: Comparison of base velocity profile $U(y)$ for different permeabilities for one and two domain approaches, when $\varepsilon_H = 0.78$, $\delta = 0.5$, $\Delta = 0.001$.

3.1 One-domain approach

The Orr–Sommerfeld (OS) boundary value problem then reads

$$
(D^2 - k^2)^2 \psi = ikRe \left[\left(\frac{U_B}{\varepsilon} - c \right) (D^2 - k^2) \psi - \frac{U_B'' \psi}{\varepsilon} + 3U_B' \frac{\varepsilon' \psi}{\varepsilon^2} + U_B \frac{\psi \varepsilon''}{\varepsilon^2} \right.
$$
$$
\left. -3U_B \frac{\psi \varepsilon'^2}{\varepsilon^3} - \left(\frac{U_B}{\varepsilon} - c \right) \frac{\varepsilon' \psi'}{\varepsilon} \right] + \frac{\varepsilon'}{\varepsilon} (D^3 - k^2 D) \psi + \frac{\varepsilon \psi''}{\kappa_x(y)} - \frac{\varepsilon k^2 \xi \psi}{\kappa_x(y)}
$$
$$
+ \varepsilon \psi' \frac{\partial}{\partial y} \left(\frac{1}{\kappa_x(y)} \right) + \frac{\varepsilon'}{\varepsilon} \psi''' + \frac{\varepsilon''}{\varepsilon} \psi'' - 2\frac{\varepsilon'^2}{\varepsilon^2} \psi'' - k^2 \frac{\varepsilon'}{\varepsilon} \psi', \tag{13a}
$$

along with the boundary conditions

$$
\psi|_0 = 0, \qquad \psi'|_0 = 0, \tag{13b}
$$
$$
\psi''|_1 + k^2 \psi|_1 = U_B''|_1 \frac{\psi|_1}{(U_B|_1 - c)}, \tag{13c}
$$
$$
\psi'''|_1 - 3k^2 \psi'|_1 = iRe\,k \left[(U_B|_1 - c)\psi'|_1 - U_B'|_1 \psi|_1 \right]
$$
$$
+ ik \left(\cot\theta \frac{Re}{Fr^2} + k^2 WeRe \right) \frac{\psi|_1}{(c - U_B|_1)}, \tag{13d}
$$

where $\varepsilon(1) = 1$, $1/\kappa(1) = 0$ has been used to simplify the continuity of the normal stress (13d). The symbol D and primes refer to derivatives with respect to the cross-stream coordinate y. The last four terms in (13a) can be referred to as the Brinkman second order correction terms. These terms arise only in the thin transitional region and are negligibly small, so in our calculation, we waived these terms [31].

The above boundary value problem is actually an eigenvalue problem for the complex phase speed c. This eigenvalue problem is solved with AUTO07p for two different inclination angles and different anisotropy ξ of the porous plate. We only looked for the surface instability modes, starting our continuation procedure at the trivial solution for $k = 0$.
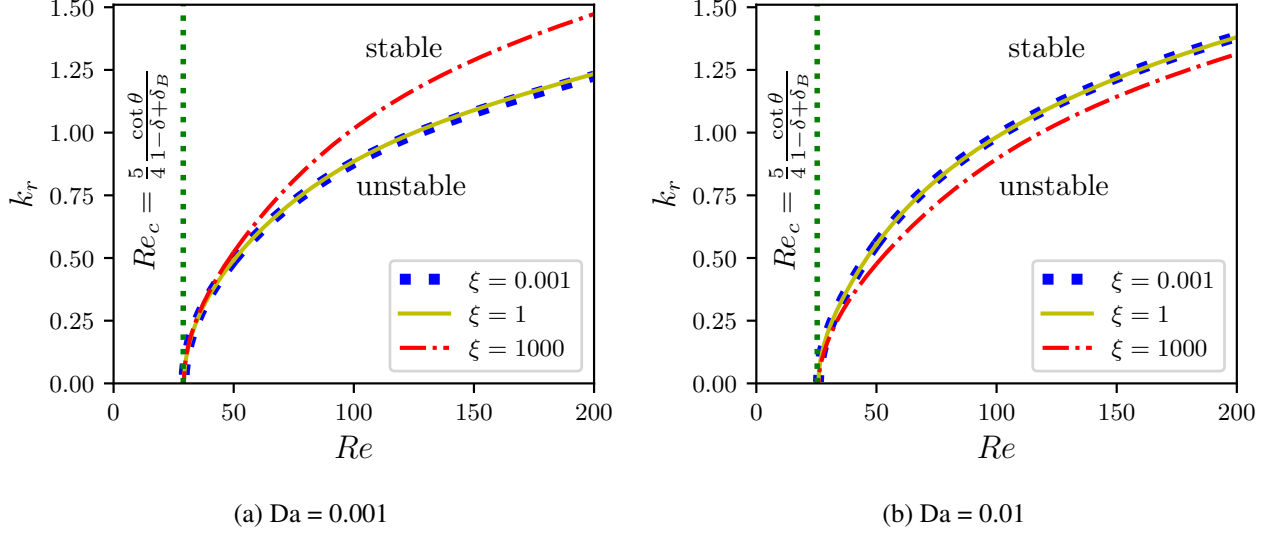
9

(a) Da = 0.001

(b) Da = 0.01

Figure 4: Marginal stability curves corresponding to Orr-Sommerfeld eigen value problem for different permeabilities and different anisotropy parameter, when $\varepsilon_H = 0.78$, $\delta = 0.5$, $\Delta = 0.001$, $\theta = 4.6°$ and $Ka = 769.8$.

3.1.1 For an inclined plane ($\theta = 4.6°$)

We first consider the spatial stability of a film on a slightly inclined porous plane for a set of parameters corresponding to an experiment by [32], $\theta = 4.6°$, $\sigma = 69$ N/m, $\rho = 1130$ kg/m^3, $\nu = 5.02 \times 10^{-6}$ m^2/s, which gives $Ka = 769.8$. We thus consider a real angular frequency $\omega = kc$, the instability of the film being signalled by a positive spatial growth rate, i.e. $-k_i > 0$. Figure 4 presents typical marginal stability curve ($-k_i = 0$) in the plane Reynolds Re versus wavenumber k_r. As expected, the threshold of the free surface instability occurs at $k = 0$ for a critical value of the Reynolds number, which depends on the inclination of the plane and the properties of the porous medium. However, anisotropy does not affect the base flow and appears in (13a) only through the product $k^2\xi$. As a consequence, the threshold of the long-wave instability of the film is not affected by the anisotropy of the porous medium and remains equal to its value for the isotropic case $\xi = 1$ studied by [1]. These authors have shown that the instability threshold closely corresponds to the case of an effective no-slip condition achieved at the bottom of the top Brinkman momentum diffusion layer, i.e. at $y = 1 - \delta + \delta_B$. In which case, the threshold of instability corresponds to a liquid film of thickness $1 - \delta + \delta_B$, which gives for our set of parameter

$$Re_c \approx \frac{5}{4} \frac{\cot\theta}{1 - \delta + \delta_B}. \tag{14}$$

The prediction (14) of the instability threshold is indicated by vertical lines on figure 4, in striking agreement with our numerical findings.

If anisotropy does not affect the instability threshold, it does displace the marginal stability curves. Figures 5 and 6 present the spatial growth rate $-k_i$, and associated real part of the phase speed at $Re = 50$ and show the influence of the anistropy parameter. At small values of the Darcy number, (Fig.4(a)), i.e. on a weakly permeable plate, the higher the anisotropy, the more unstable the film flow is. An opposite phenomenon is noticed at high values of the Darcy number, i.e. on a more permeable plate (see Fig.4(b)). This dual behaviour of anisotropy is illustrated in Fig.5, which shows the spatial growth rate of instability. The isotropic case ($\xi = 1$) is compared to a high cross-stream permeability ($\xi = 0.001$) and a low cross-stream permeability ($\xi = 1000$) cases. Anisotropy affects the growth rate and phase velocity only for the largest values of the wavenumber k_r, again owing to the fact that ξ is grouped with k^2 in a single term of (13a). However, a film flowing on a porous substrate with high cross-stream permeability, i.e. $\xi \ll 1$, presents stability which is equivalent to a flow on an isotropic porous medium as the marginal stability curves, growth rates, and phase speeds are identical at $\xi = 1$ and $\xi = 0.001$.
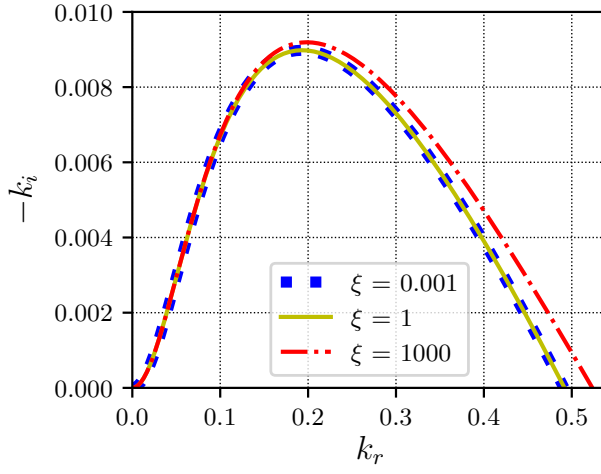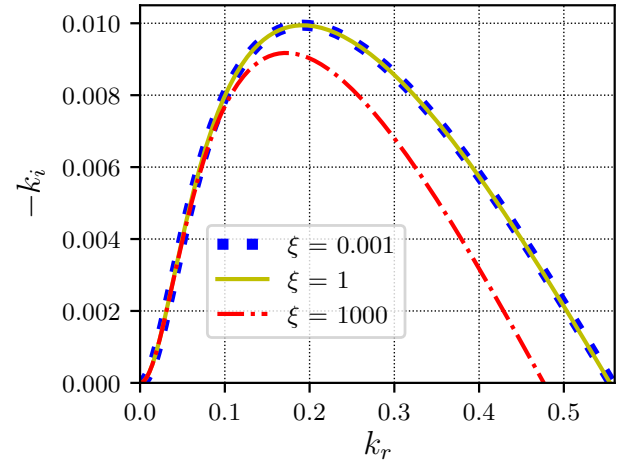
10

(a) Da = 0.001

(b) Da = 0.01

Figure 5: Spatial growth rate for different permeabilities and different anisotropy parameter, when $\varepsilon_H = 0.78$, $\delta = 0.5$, $\Delta = 0.001$, $\theta = 4.6°$, $Ka = 769.8$ and for $Re = 50$.
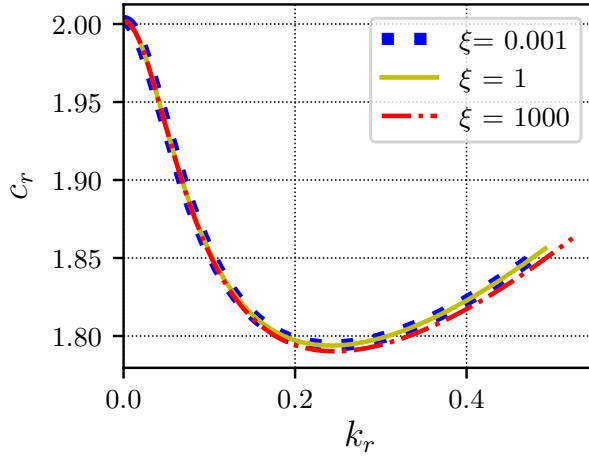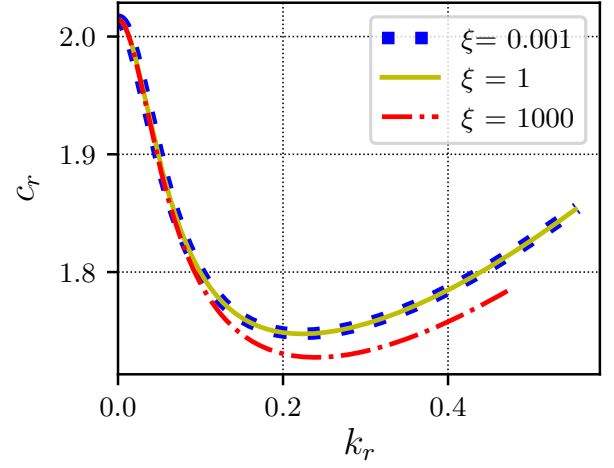

(a) Da = 0.001

(b) Da = 0.01

Figure 6: Phase speed in (k_r, c_r) plane for different permeabilities and different anisotropy parameters, when $\varepsilon_H = 0.78$, $\delta = 0.5$, $\Delta = 0.001$, $\theta = 4.6°$, $Ka = 769.8$ and for $Re = 50$.
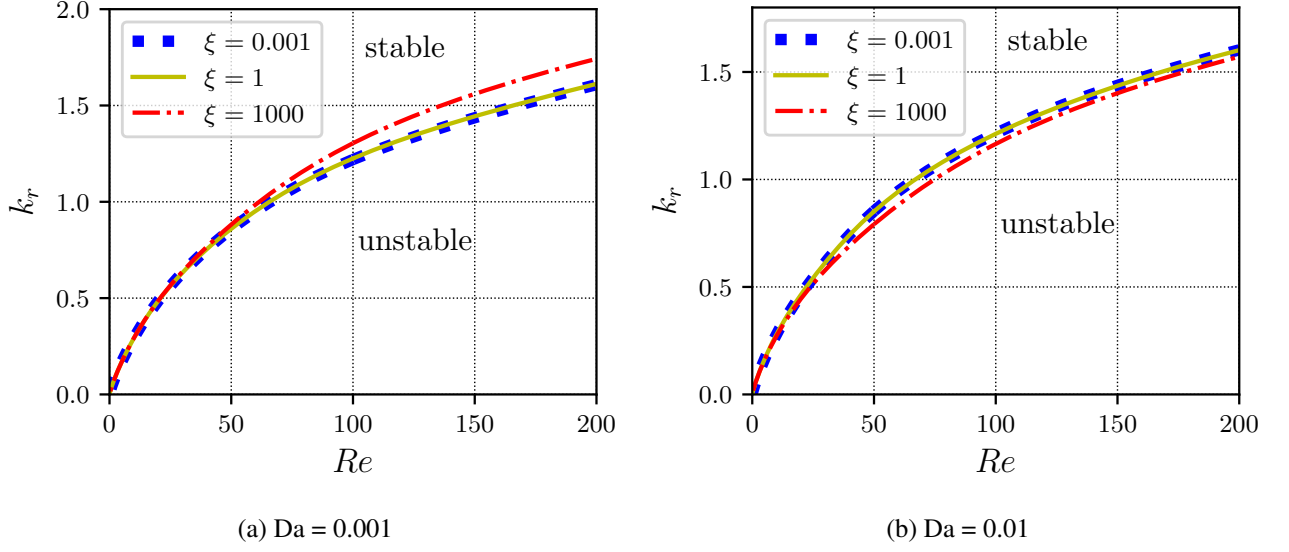
11

(a) Da = 0.001

(b) Da = 0.01

Figure 7: Marginal stability curves corresponding to Orr-Sommerfeld eigenvalue problem for different permeabilities and different anisotropy parameter for a vertical plate ($\theta = 90°$), when $\varepsilon_H = 0.78$, $\delta = 0.5$, $\Delta = 0.001$, and $Ka = 769.8$.

3.1.2 For a vertical plane

When the flow occurs over a vertical porous plate, the effect of anisotropy is weaker. However, the dual behaviour of the anisotropy parameter remains in this case similar to the inclined plane case as can be observed in Figure 7 which presents the marginal stability curves. As for the slightly inclined plane, the stability analysis departs from the isotropic case $\xi = 1$ only at large values of ξ corresponding to a very low cross-stream permeability.

3.2 Two-domain approach

Let us now turn to the two-domain approach and compare the stability results based on the one-domain and two-domain approaches. The linear stability analysis next yields an Orr-Sommerfeld system of equations to be solved:

$$\psi'''' - 2k^2\psi'' + k^4 = Reik\left[(U_B - c)\left(\psi'' - k^2\psi\right) - U_B''\psi\right], \tag{15}$$

$$\psi_p'''' - 2k^2\psi_p'' + k^4 = -Reik\left(\psi_p'' - k^2\psi_p\right) + \frac{\varepsilon}{Da}\left[\psi_p'' - k^2\xi\psi_p\right], \tag{16}$$

with the boundary conditions:

$$\psi_p|_0 = 0, \qquad \psi_p'|_0 = 0, \tag{17}$$

$$\psi_p|_\delta = \psi|_\delta, \qquad \psi_p'|_\delta = \psi'|_\delta, \tag{18}$$

$$\frac{1}{\varepsilon}\partial_{yy}\psi_p|_\delta - \partial_{yy}\psi|_\delta = \frac{\beta}{\sqrt{Da}}\psi_p'|_\delta, \tag{19}$$

$$\psi'''|_\delta - 3k^2\psi'|_\delta - ikRe\left[\left(U_B|_\delta - c\right)\psi'|_\delta - U_B|_\delta\psi|_\delta\right]$$
$$= \frac{1}{\varepsilon}\left(\psi_p'''|_\delta - 3k^2\psi_p'|_\delta\right) + \frac{1}{\varepsilon}ikRe\psi_p|_\delta - \frac{1}{Da}\psi_p'|_\delta, \tag{20}$$

(a) Da = 0.001, $\beta = 0.16$
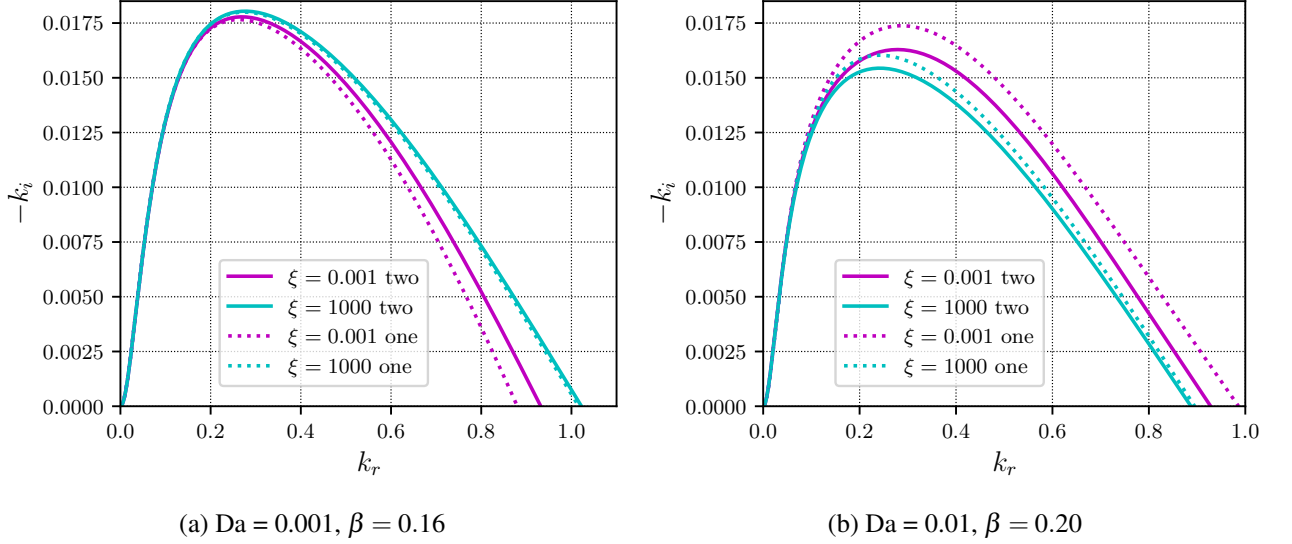
(b) Da = 0.01, $\beta = 0.20$

Figure 8: Comparison of spatial growth rates from one-domain (one) and from two-domain (two) approaches for different permeabilities and different anisotropy parameters, when $\varepsilon_H = 0.78$, $\delta = 0.5$, $\Delta = 0.001$, $\theta = 4.6°$, $Ka = 769.8$ and for $Re = 100$.

$$\psi''|_1 + k^2\psi|_1 = U_B''|_1 \frac{\psi|_1}{(U_B|_1 - c)}, \tag{21}$$

$$\psi'''|_1 - 3k^2\psi'|_1 = ikRe\left[(U_B|_1 - c)\,\psi'|_1\right] + ik\left(\frac{Re}{Fr^2}\cot\theta + k^2WeRe\right)\frac{\psi|_1}{(c - U_B|_1)}, \tag{22}$$

where, ψ and ψ_p denote the amplitudes of the stream functions in the liquid and porous regions.

Figures 8 and 9 compare the growth rates and marginal stability curves obtained from the two-domain approach to the one-domain results for $\theta = 4.6°$ (similar results are obtained for a vertical wall and therefore are not shown). For low to moderate Reynolds numbers, one-domain and two-domain approaches are in excellent agreement. For higher Reynolds numbers, deviations are observed only at low values of the anisotropy parameter. Surprisingly, the two-domain approach seems to underestimate the growth rate and range of unstable wavenumbers at low values of the Darcy number, whereas the opposite is observed at higher values of Da. We note that the observed discrepancies cannot result from the base flow solutions U_B which are in striking agreement (cf. figure 3). Comparing one-domain and two-domain systems of equations, the differences in results shall stem from either (i) the neglect of the convective terms in the porous layer or (ii) the stress boundary conditions. Since U_B is much smaller than the phase speed c in the porous medium, the neglect of convective terms in the momentum balance shall not explain the observed discrepancy. Instead, a more obvious candidate is the fact that the viscous stresses in the normal stress balance are assumed to be discontinuous in equation (6j). Besides, (6j) does not involve the gradients of the cross-stream velocity, which are not negligible if the cross-stream dimensionless permeability Da/ξ is large. However, the one-domain and two-domain approaches agree remarkably well, which validates the approaches chosen so far. In particular, the non-trivial influence of ξ on the marginal stability curves found with the one-domain approach is also observable with the two-domain approach (see figure 9).

3.3 Slip boundary condition

[9] argued that a Navier slip boundary condition could model the influence of the flow in the porous medium at the porous-fluid interface, which is then assumed to be impermeable:

$$l_s\partial_y u = u \quad \text{at} \quad y = \delta, \tag{23}$$

13

(a) Da = 0.001, $\beta = 0.16$
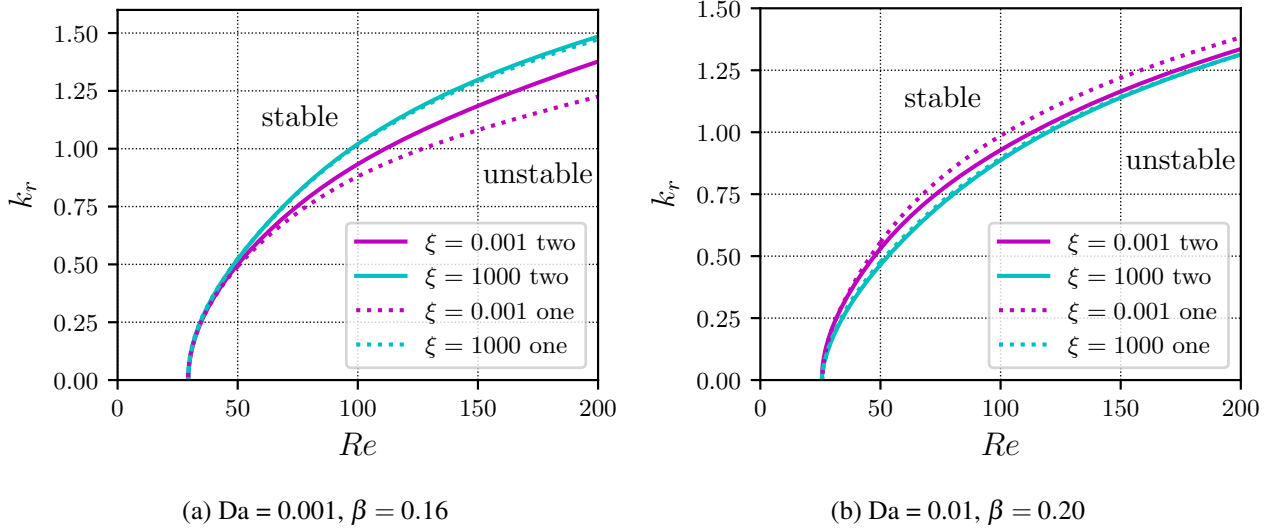
(b) Da = 0.01, $\beta = 0.20$

Figure 9: Comparisons of marginal stability curves from one-domain (one) and from two-domain (two) approaches for different permeabilities and different anisotropy parameters, when $\varepsilon_H = 0.78$, $\delta = 0.5$, $\Delta = 0.001$, $\theta = 4.6°$, and $Ka = 769.8$.

where l_s is a dimensionless slip length. The corresponding Orr-Somerfeld linear stability eigenvalue problem reduces to (15) with the boundary conditions

$$\psi|_0 = 0, \qquad l_s \psi''|_0 - \psi'|_0 = 0. \tag{24}$$

This approach dramatically simplifies the treatment of the porous layer but neglects the mass transfer from the porous medium to the liquid film and the cross-stream velocity in the porous medium. In the remainder of this section, we wish to challenge this approximation, referred to as the slip model, as well as the effective no-slip boundary condition that has been proposed by [1] (see below).

3.4 Discussion

Having validated our linear stability analysis by comparisons to the two-domain approach (§3.2), we challenge Pascal's Navier slip approximation and revisit the argument presented by [1] that the stability of a film on a porous media is equivalent to the stability of a liquid film on an impermeable effective boundary located at $y = \delta - \delta_B$ where the Brinkman layer thickness is defined by $\delta_B = \sqrt{Da/\varepsilon_H}$, hereinafter referred to as the "no-slip model".

Figure 10 compares the Orr-Sommerfeld marginal stability curves obtained with the one-domain approach to the corresponding ones for the slip model and the effective no-slip model. For the slip model, the dimensionless slip length has been adjusted in order that the base flow profile verifies the relation (9) which gives

$$l_s = \delta_B + \frac{\delta_B^2}{2(H - \delta)}. \tag{25}$$

As expected, at a low permeability ($Da = 10^{-4}$) and high anisotropy parameter ($\xi = 1000$), all curves collapse on a single one as the extension of the Brinkman momentum layer $\delta_B \propto \sqrt{Da}$ in the porous layer is relatively limited, and the mass exchange between the porous medium and liquid film is impaired at low cross-stream permeability Da/ξ. Results from the slip and the no-slip models are always in good agreement. However, the slip model tends to predict a wider range of unstable wavenumbers than the no-slip model. This is likely due to the fact that the no-slip model allows for some limited mass exchange at the porous-liquid interface $y = \delta$, whereas this interface is considered impermeable in the case of the slip model. Consequently, we expect a

(a) Da = 0.0001

(b) Da = 0.001
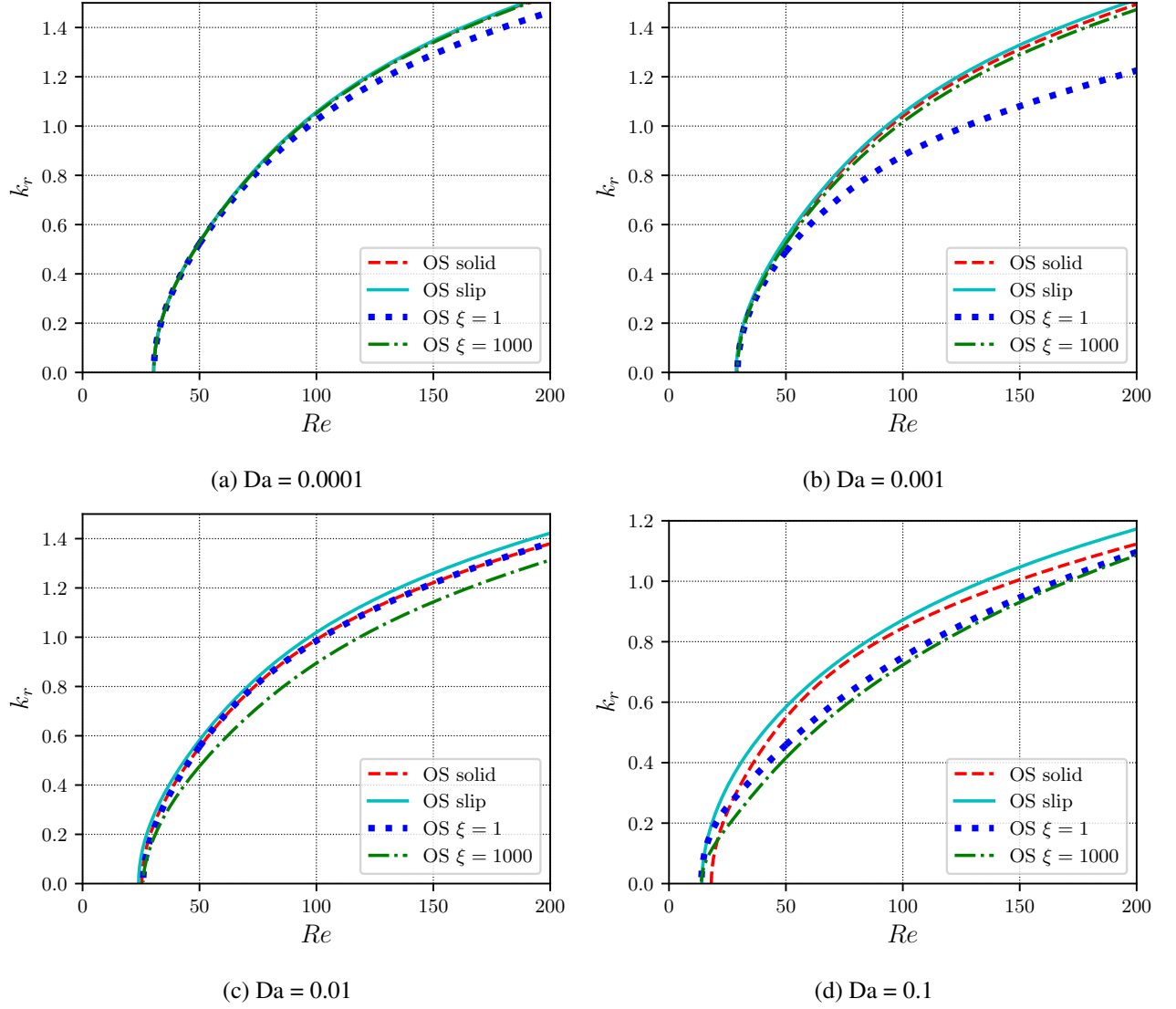
(c) Da = 0.01

(d) Da = 0.1

Figure 10: Comparisons of marginal stability curves for a film flow over a solid wall at $y = \delta - \delta_B$ (OS solid), film flow over slippary inclined plane (OS slip) and one-domain porous medium, for different permeabilities and different anisotropy parameters when $\varepsilon_H = 0.78$, $\delta = 0.5$, $\Delta = 0.001$, $\theta = 4.6°$ and $Ka = 769.8$.

slightly more effective attenuation of the waves by diffusion in the case of the no-slip model. At $Da = 0.001$ (panel b in figure 10), the no-slip model, slip model and the one-domain approach with a high anisotropy parameter $\xi = 1000$ are again in close agreement. This is expected since the low cross-permeability Da/ξ prevents a significant flow in the cross-stream direction in the porous medium, which is thus likely to be nearly equivalent to the effective impermeable wall at $y = \delta - \delta_B$ (no-slip model). However, the marginal stability curve for the isotropic case significantly departs from the slip and the no-slip models, which signals that the cross-stream flow in the porous medium plays a significant role in reducing the range of unstable wavenumbers. At large values of the Darcy number ($Da = 0.01$ and $Da = 0.1$), the curves are again relatively close. We note that for these values of the Darcy number, the nearly uniform section of the base flow profile in the bulk of the porous medium (Darcy region) may be suppressed, the drag from the solid structure on the flow u/k_x being weaker than the shear viscous forces $\partial_{yy}u$. Consequently, the flows in the liquid film and the porous substrate become similar, and the film instability behaves as if the liquid film extends on the entire fluid domain, the porous medium being removed. We note that the marginal stability curves for the slip and no-slip models are almost always above the others, which indicates that the permeability of the liquid-porous interface has a stabilising effect except close to the instability threshold.

Finally, following [1], we recast the results of our stability analysis using dimensional units. Figure 11 presents the marginal stability curves when recast in the plane dimensional flow rate q_N versus dimensional frequency. For a thin porous layer ($\delta = 0.1$), we exactly recover the results obtained by [1]. The curves all collapse onto a single curve irrespectively of the value of the Darcy number. This curve corresponds to the stability of a liquid film on a solid plate. Following [1], we conclude that for thin porous layers, a film flowing on a porous substrate follows the same dynamics as a film on a solid impermeable substrate. However, for a thicker porous region ($\delta = 0.5$), the marginal stability curves present noticeable differences, the permeability of the porous medium significantly enhancing the stability of the flow, except close to the instability threshold.

Nevertheless, this effect is not monotonous, and we observe again that varying the anisotropy parameter may modify the relative location of the marginal stability curves (compare the marginal curves for $Da = 0.001$ and $Da = 0.01$). At a large permeability ($Da = 0.1$), the instability occurs at a lower flow rate than for the solid-wall situation. We suggest that this slight discrepancy on the instability threshold is a consequence of the large difference observed for the velocity profiles (see figure 2). Our results suggest that the mass exchange at the liquid-porous boundary plays a role in attenuating the instability far to its threshold.

4 Weighted residual modelling

In this section, we follow the strategy proposed by [1] to derive a semi-analytic model to capture the long-wave wavy regime of the film flow. The procedure relies on choosing a set of variables whose evolution mimics the complete dynamics of the flow. [1] chose the film height H and the local flow rate $q = \int_0^H u\,dy$ to characterize the flow evolution. We show in sections §4.4 and §5 that this strategy is inadequate when a low cross-stream permeability of the porous medium (high values of ξ) is considered. As we underline below, this deficiency results from a decoupling between the flow in the porous and liquid regions.

4.1 Three-equation model

We introduce two different flow rates to allow for the velocity distribution in the porous medium to be decoupled from the one in the liquid. We define

$$q_l = \int_0^H Id_l u\,dy \quad \text{and} \quad q_p = \int_0^H Id_p u\,dy, \tag{26a}$$

$$\text{with} \quad Id_l = 0.5 + 0.5\tanh[(y-\delta)/\Delta], \tag{26b}$$

$$Id_p = 0.5 - 0.5\tanh[(y-\delta)/\Delta], \tag{26c}$$

so that $Id_l = 1$ and $Id_p = 0$ in the liquid region and conversely $Id_l = 0$ and $Id_p = 1$ in the porous medium. Thus, $q_l \approx \int_\delta^H u\,dy$ is the local discharge of liquid above the porous-liquid interface $y = \delta$ and $q_p \approx \int_0^\delta u\,dy$ is the rate
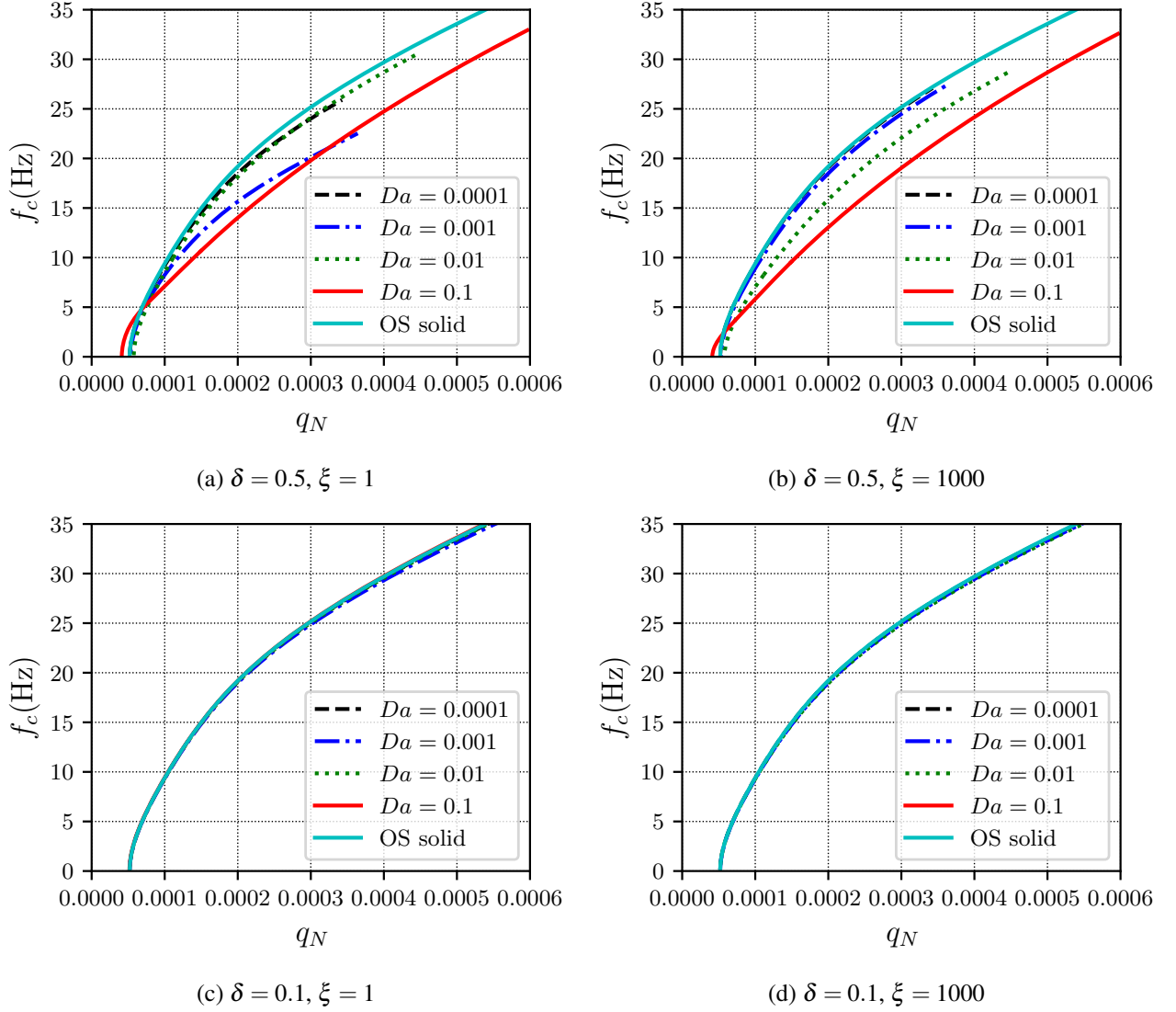
Figure 11: Marginal stability curves for different thicknesses of an anisotropic porous layer for different Darcy values and different ξ values: dimensional cut-off frequency f_c versus dimensional flow rate q_N, for $\varepsilon_H = 0.78$, (a), (b) $\delta = 0.5$, (c), (d) $\delta = 0.1$, $\Delta = 0.001$, $\theta = 4.6°$. 'OS solid' refers to an impermeable no-slip boundary.

of liquid flowing in the porous medium. Since $Id_l + Id_p = 1$, the total flow rate q is equal to the sum of q_l and q_p. Integrating the continuity equation (3a) across the fluid and the porous layer, we get the exact mass balance

$$\partial_t H + \partial_x(q_l + q_p) = 0. \tag{27}$$

Two evolution equations can be obtained for q_l and q_p using the weighted residual technique once a velocity profile is assumed (closure assumption). We consider slow space and time evolutions $\partial_{x,t} \sim \gamma$ where γ is a formal small parameter that counts the order of derivation with respect to time and space of the different variables. The velocity distribution across the porous and fluid layers is assumed to remain close to the Nusselt flat-film distribution, deviations from the Nusselt profile being $O(\gamma)$ corrections induced by the free surface deformations. We write

$$u = q_l(x,t) f_l(y;H(x,t)) + q_p(x,t) f_p(y;H(x,t)) + \gamma \tilde{u}. \tag{28}$$

We use the linearity of the equations (8) verified by the base flow to write the velocity profile as the superposition of two solutions.

$$L f_l = -C_{ll} Id_l - C_{lp} Id_p, \tag{29a}$$
$$L f_p = -C_{pl} Id_l - C_{pp} Id_p, \tag{29b}$$

where L refers again to the operator $\partial_{yy} - (\varepsilon/\kappa_x) Id$. For convenience, we rewrite the above equation in a condense format using Einstein notations as

$$L f_i = -C_{ij} Id_j, \tag{29c}$$

where $i, j = l$ or p and repetition of indices indicates a summation. Associated boundary conditions are

$$f_l(0) = f_p(0) = 0 \quad \text{and} \quad \partial_y f_l(H) = \partial_y f_p(H) = 0. \tag{29d}$$

The constants C_{ij} are adjusted to verify the integral constraints

$$\int_0^H Id_i f_j dy = \delta_{ij}, \tag{29e}$$

implied by the definition (26) of the variables q_l and q_p. Here δ_{ij} refers to the Kronecker delta function. Constants C_{ij} are therefore dependent on the geometry of the porous medium and therefore functions of the film height H. The decomposition (28) is made unique with the two gauge conditions

$$\int_0^H Id_i \tilde{u} dy = 0, \tag{29f}$$

which guaranty that the decomposition (28) verify the definitions (26) of the flow rates q_l and q_p in the liquid and porous layers.

The momentum balances (3b) and (3c) are next simplified within the framework of the long-wave expansion to yield a Prandtl-like equation after elimination of the pressure field. From the continuity equation (3a) we get $v = -\int_0^y \partial_x u \, dy = O(\gamma)$, so that inertial terms in the cross-stream momentum balance equation (3c) are $O(\gamma^2)$ and can be omitted. Integration of (3c) thus gives

$$Re\,p = 2\partial_y v\,|_H - Re We \partial_{xx} H + \int_H^y \frac{1}{\varepsilon(y)} L v \, dy + (1-\xi) \int_H^y \frac{v}{\kappa} dy - \frac{Re}{Fr^2} \cot\theta (y-H) + O(\gamma^2), \tag{30}$$

where the leading order contribution from surface tension, $-We Re \partial_{xx} H$, has been retained, although it is formally $O(\gamma^2)$, since surface tension prevents the breaking of waves. Substituting (30) into (3b) we get the boundary layer equation:

$$Re\left[u_t + \frac{1}{\varepsilon}(uu_x + vu_y) + uv\frac{\partial}{\partial y}\left(\frac{1}{\varepsilon}\right)\right] = \varepsilon\left[\frac{Re}{Fr^2}(1 - \cot\theta H_x) + Re We H_{xxx}\right]$$
$$-\varepsilon(y)\frac{\partial}{\partial x}\int_H^y \frac{1}{\varepsilon} L v \, dy - \varepsilon(1-\xi)\frac{\partial}{\partial x}\int_H^y \frac{v}{\kappa} dy + u_{xx} + Lu + 2\varepsilon\frac{\partial}{\partial x}(u_x\,|_H), \tag{31}$$

with the associated boundary conditions

$$u \mid_0 = v \mid_0 = 0, \tag{32a}$$

$$\partial_y u \mid_H = 4\partial_x u \mid_H \partial_x H - \partial_x v \mid_H, \tag{32b}$$

$$v \mid_H = \partial_t H + u \mid_H \partial_x H. \tag{32c}$$

Following the weighted residual method, we insert (28) into the truncated momentum balance (31) and average it with weights which verify

$$Lw_i = -\frac{Re}{Fr^2}Id_i, \qquad w_i(0) = \partial_y w_i(H) = 0. \tag{33}$$

This choice of weights enable to make use of the gauge conditions (29f) to get rid of the $O(\gamma)$ corrections arising from the evaluation of the viscous terms

$$\int_0^H w_i L u dy = w_i(H)\partial_y u|_H + \int_0^H Lw_i u dy = w_i(H)\left[4u_x \mid_H H_x - v_x \mid_H\right] - \frac{Re}{Fr^2}q_i. \tag{34}$$

We finally obtain two averaged momentum balances of the form:

$$
\begin{aligned}
S_i^{(k)}\partial_t q_i &= -F_{ij}^{(k)}\frac{q_j}{H}\partial_x q_i + G_{ij}^{(k)}\frac{q_j q_i}{H^2}\partial_x H + \frac{1}{Fr^2}\left[I^{(k)}b(H)H - \frac{q_k}{H^2}\right] \\
&\quad + \frac{1}{Re}\left[(J_i^{(k)} + \xi \tilde{J}_i^{(k)})\frac{q_i}{H^2}(\partial_x H)^2 - (K_i^{(k)} + \xi \tilde{K}_i^{(k)})\frac{\partial_x q_i \partial_x H}{H}\right. \\
&\quad \left. -(L_i^{(k)} + \xi \tilde{L}_i^{(k)})\frac{q_i}{H}\partial_{xx} H + (M_i^{(k)} + \xi \tilde{M}_i^{(k)})\partial_{xx}q_i\right],
\end{aligned}
\tag{35}
$$

where $b(H) = 1 - \cot\theta\partial_x H + WeFr^2\partial_{xxx}H$ combines the gravity acceleration and the pressure gradient which drive the flow. Equations (27) and (35) form a a three-equation system of evolution equations for the three variables H, q_l and q_p.

All fifty-four coefficients involved in (35) depend on the geometry and therefore on H. The expressions of the coefficients are given in Appendix §A. We used the software AUTO07p to compute (29), (33), (51) and tabulated the coefficients (52) as function of the film height H.

The derived system of equations is consistent up to order γ for convective terms and up to $O(\gamma^2)$ for diffusion ones. We underline that consistency up to $O(\gamma)$ is a requisite to ensure that the instability threshold is captured adequately. Inclusion of viscous diffusion terms enables to recover correctly the amplitude of the capillary ripples, which precede hump waves and solitary waves and govern their dynamics.

4.2 Two-equation models

In the limit of small cross-stream permeability ($\xi \gg 1$), we expect the cross-stream velocity component v to be small in the porous medium so that the streamwise velocity component u is nearly constant in the porous medium. Consequently, we expect q_p to be nearly constant in that case. This is supported by the fact that the coefficient $\tilde{M}_p^{(p)}$ is found to be relatively large, and we expect an efficient diffusion of q_p at large values of ξ.

Assuming $q_p = cst$ or $q_p \ll 1$, the model reduces to two evolution equations for H and q_l. From (35), we have

$$
\begin{aligned}
S_l^{(l)}\partial_t q_l &= -F_{lj}^{(l)}\frac{q_j}{H}\partial_x q_l + G_{ij}^{(l)}\frac{q_j q_i}{H^2}\partial_x H + \frac{1}{Fr^2}\left[I^{(l)}b(H)H - \frac{q_l}{H^2}\right] \\
&\quad + \frac{1}{Re}\left[(J_i^{(l)} + \xi \tilde{J}_i^{(l)})\frac{q_i}{H^2}(\partial_x H)^2 - (K_l^{(l)} + \xi \tilde{K}_l^{(l)})\frac{\partial_x q_l \partial_x H}{H}\right. \\
&\quad \left. -(L_i^{(l)} + \xi \tilde{L}_i^{(l)})\frac{q_i}{H}\partial_{xx} H + (M_l^{(l)} + \xi \tilde{M}_l^{(l)})\partial_{xx}q_l\right],
\end{aligned}
\tag{36}
$$

The two-equation model (27, 36) shall be contrasted with the two-equation approach adopted in [1]. Choosing the film elevation H and the total flow rate $q = q_l + q_p$ as the set of variables, a set of evolution equations can be obtained with the above weighted residual method with the ansatz

$$u = q f(y; H) + \gamma \tilde{u}, \tag{37}$$

where f corresponds to the base flow profile U_B and verifies

$$L f = -C, \quad f(0) = 0, \quad \partial_y f(H) = 0, \quad \int_0^H f \, dy = 1. \tag{38}$$

The same procedure as the one outline in §4.1 is then followed with a weight defined by

$$L w = -\frac{Re}{Fr^2}, \quad \partial_y w(H) = 0. \tag{39}$$

Integrating (31) with the weight w then leads to

$$\begin{aligned}
S(H)\partial_t q = &-F(H)\frac{q}{H}\partial_x q + G(H)\frac{q^2}{H^2}\partial_x H + \frac{1}{Fr^2}\left[I(H)b(H)H - \frac{q}{H^2}\right] \\
&+ \frac{1}{Re}\left[\left(J(H) + \xi\tilde{J}(H)\right)\frac{q}{H^2}(\partial_x H)^2 - \left(K(H) + \xi\tilde{K}(H)\right)\frac{\partial_x q\,\partial_x H}{H}\right. \\
&\left. - \left(L(H) + \xi\tilde{L}(H)\right)\frac{q}{H}\partial_{xx}H + \left(M(H) + \xi\tilde{M}(H)\right)\partial_{xx}q\right].
\end{aligned} \tag{40}$$

The expressions of the coefficients from $S(H)$ to $\tilde{M}(H)$ correspond to (51) and (52) once indices have been dropped out. For an isotropic porous medium $\xi = 1$, the averaged momentum balance (40) is fully identical to the corresponding one obtained by [1] as the differences in the expressions of the coefficients arise from a different choice of writing of the ansatz (37) which do not affect the result.

For $Da \ll 1$, numerical comparisons of the coefficients $S(H)$ to $\tilde{M}(H)$ to their counterparts, $S_l(H)^{(l)}$ to $\tilde{M}_l(H)^{(l)}$, present a relatively good agreement as the contributions of the velocity distribution and weight in the porous medium are then weak. We therefore expect that the solutions of the three-equation model (27, 35), to the two-equation model (27, (40)), and to Samanta's isotropic two-equation formulation lie close one to the other at low values of Da and moderate values of ξ, for which the assumption $q_p \ll 1$ holds and the contributions of the porous medium to the elongational viscous diffusion terms ($\xi\tilde{L}_l^{(l)}$ and $\xi\tilde{M}_l^{(l)}$) are moderate.

4.3 Approximation

In order to get a more handable model, we propose here a drastic simplification of our modelling attempt. This simplification relies on a polynomial approximation of the velocity profiles f_i and weights w_i (i referring to either l or p). To proceed, we separate the flow in three regions: a Brinkman sublayer of thickness $\delta_B = \sqrt{Da/\varepsilon_H}$ at the bottom of the porous layer, a uniform-flow Darcy region in the bulk of the porous layer from $y = \delta_B$ to $y = \delta - \delta_B$, an effective liquid layer from $y = \delta - \delta_B$ to the top of the film flow $y = H$. We thus approach f_i and w_i as

$$\begin{aligned}
f_i &= a_i y, \quad w_i = a_{wi} y, \quad \text{for} \quad 0 \le y \le \delta_B, \\
f_i &= a_i \delta_B, \quad w_i = a_{wi}\delta_B, \quad \text{for} \quad \delta_B \le y \le \delta - \delta_B, \\
f_i &= a_i \delta_B + b_i \tilde{U}_B, \quad w_i = a_{wi}\delta_B + b_{wi}\tilde{U}_B, \quad \text{for} \quad y \ge \delta - \delta_B,
\end{aligned} \tag{41}$$

where $\tilde{U}_B$ is given by (9). This approximation implies that the operator L reduces to ∂_{yy} in the Brinkman sublayers $\delta - \delta_B \le y \le \delta$ and to $-(\varepsilon_H/Da)Id$ in the Darcy layer, or bulk, of the porous layer. This approximation also assumes that the transitional layer has a negligible thickness and that the thickness of the momentum boundary layers δ_B is small. Approximation (41) yields explicit expressions of the coefficients (52), of which we retain

only the leading order contributions or up to $O(\delta_B)$. Additionally, the flow rate in the porous layer q_p can be inferred to be proportional to the Darcy number so that $q_p = O(\delta_B^2)$ is small and the corresponding coefficients are truncated to their leading order with respect to δ_B. Since the velocity distribution in the liquid layer and the top Brinkman layer $\delta \leq y \leq \delta - \delta_B$ is close to the velocity distribution of a liquid film on a solid interface at $y = \delta - \delta_B$, we introduce the effective film thickness $h = H - \delta + \delta_B$ and the effective thickness of the porous medium $\tilde{\delta} = \delta - \delta_B$. We thus obtain explicit expressions of the coefficients that are listed in Appendix §B.

The averaged momentum balances (36) thus simplify into

$$
\begin{aligned}
\partial_t q_l - \frac{h}{6\tilde{\delta}} \partial_t q_p = {}& \left(-\frac{17}{7}\frac{q_l}{h} + \frac{3}{7}\frac{q_p}{\tilde{\delta}} \right) \partial_x q_l + \left[\left(\frac{1}{2} - \frac{3}{7}\frac{h}{\tilde{\delta}} \right) \frac{q_l}{h} + \left(\frac{11}{42}\frac{h}{\tilde{\delta}} + \frac{15}{16} \right) \frac{q_p}{\tilde{\delta}} \right] \partial_x q_p \\
& + \left[\frac{9}{7}\frac{q_l^2}{h^2} - \frac{1}{7}\frac{q_l q_p}{h\tilde{\delta}} - \frac{1}{7}\frac{q_p^2}{\tilde{\delta}^2} \right] \partial_x h + \frac{1}{Fr^2} \left[\frac{5h}{6}b(h) - \frac{5(1-\tilde{\delta})^2}{4h^2}q_l \right] \\
& + \frac{1}{Re} \left\{ 4\frac{q_l(\partial_x h)^2}{h^2} - \frac{9}{2}\frac{\partial_x q_l \partial_x h}{h} + \frac{1}{2}\frac{\partial_x q_p \partial_x h}{\tilde{\delta}} - 6\frac{q_l}{h}\partial_{xx}h + \frac{3}{2}\frac{q_p}{\tilde{\delta}}\partial_{xx}h \right. \\
& \left. + \frac{9}{2}\partial_{xx}q_l + \left[\frac{5}{4} - \frac{3h}{4\tilde{\delta}} \right]\partial_{xx}q_p \right\},
\end{aligned}
\tag{42a}
$$

$$
\begin{aligned}
\partial_t q_l + \partial_t q_p = {}& -\left(\frac{12}{5}\frac{q_l}{h} - \frac{2}{5}\frac{q_p}{\tilde{\delta}} \right) \partial_x q_l + \left(\frac{2}{5}\frac{q_l}{\tilde{\delta}} - \frac{4\varepsilon_H h + 5\tilde{\delta}(2+3\varepsilon_H)}{10\tilde{\delta}\varepsilon_H}\frac{q_p}{\tilde{\delta}} \right) \partial_x q_p \\
& + \left(\frac{6}{5}\frac{q_l^2}{h^2} - \frac{1}{5}\frac{q_p^2}{\tilde{\delta}^2} \right) \partial_x h + \frac{1}{Fr^2} \left[(h + \tilde{\delta}\varepsilon_H)b(h) - \frac{(1-\tilde{\delta})^2\varepsilon_H}{2Da}q_p \right] \\
& + \frac{1}{Re} \left\{ \left[\frac{3(2h + \tilde{\delta}\varepsilon_H)}{h} - 3\xi\frac{\tilde{\delta}^2}{h^2} \right] \frac{q_l(\partial_x h)^2}{h^2} + \xi\frac{\tilde{\delta}q_p(\partial_x h)^2}{h^3} \right. \\
& + \left[-\frac{3(2h + \tilde{\delta}\varepsilon_H)}{h} + 2\xi\frac{\tilde{\delta}^2}{h^2} \right]\frac{\partial_x q_l \partial_x h}{h} + \frac{(h^2 - \xi\tilde{\delta}^2)}{\tilde{\delta}h}\frac{\partial_x q_p \partial_x h}{h} \\
& + \left[-\frac{3(4h + \tilde{\delta}\varepsilon_H)}{2h} + \xi\frac{\tilde{\delta}^2}{h^2} \right]\frac{q_l}{h}\partial_{xx}h + \left[\frac{3}{2} - \xi\frac{\tilde{\delta}^2}{2h^2} \right]\frac{q_p}{\tilde{\delta}}\partial_{xx}h \\
& + \frac{1}{2} \left[9 + \frac{3\tilde{\delta}\varepsilon_H}{h} - \frac{\xi\tilde{\delta}^2}{h^2} \right]\partial_{xx}q_l \\
& \left. + \left[\frac{1}{2}\left(4 + \varepsilon_H - \frac{h}{\tilde{\delta}} \right) + \frac{\xi}{3}\frac{\tilde{\delta}^2\varepsilon_H}{Da} \right]\partial_{xx}q_p \right\}.
\end{aligned}
\tag{42b}
$$

Completed by the mass balance rewritten in terms of h, q and q_p i.e.

$$
\partial_t h + \partial_x(q_l + q_p) = 0.
\tag{43}
$$

We note that the influence of the cross-stream dimensionless permeability ξ/Da appears only in the approximate momentum balance for the porous medium (42b) as the coefficients $\tilde{J}_j^{(l)}$, $\tilde{K}_j^{(l)}$, $\tilde{L}_j^{(l)}$ and $\tilde{M}_l^{(l)}$ are of order $O(\delta_B^3)$, $\tilde{M}_p^{(l)} = O(\delta_B)$ and $q_p = O(\delta_B^2)$.

System (42) can be further simplified by considering $q_p = O(Da)$ and keeping leading order terms at the

r.h.s. of (42) considering $Da \ll 1$. We thus obtain.

$$
\partial_t q_l - \frac{h}{6\tilde{\delta}}\partial_t q_p = -\frac{17}{7}\frac{q_l}{h}\partial_x q_l + \frac{9}{7}\frac{q_l^2}{h^2}\partial_x h + \frac{1}{Fr^2}\left[\frac{5h}{6}b(h) - \frac{5(1-\tilde{\delta})^2}{4h^2}q_l\right]
$$
$$
+\frac{1}{Re}\left\{4\frac{q_l(\partial_x h)^2}{h^2} - \frac{9}{2}\frac{\partial_x q_l \partial_x h}{h} - 6\frac{q_l}{h}\partial_{xx}h + \frac{9}{2}\partial_{xx}q_l\right\}, \tag{44a}
$$

$$
\partial_t q_l + \partial_t q_p = -\frac{12}{5}\frac{q_l}{h}\partial_x q_l + \frac{6}{5}\frac{q_l^2}{h^2}\partial_x h + \frac{1}{Fr^2}\left[(h+\tilde{\delta}\varepsilon_H)b(h) - \frac{(1-\tilde{\delta})^2 \varepsilon_H}{2Da}q_p\right]
$$
$$
+\frac{1}{Re}\left\{\left[\frac{3(2h+\tilde{\delta}\varepsilon_H)}{h} - 3\xi\frac{\tilde{\delta}^2}{h^2}\right]\frac{q_l(\partial_x h)^2}{h^2} + \left[-\frac{3(2h+\tilde{\delta}\varepsilon_H)}{h} + 2\xi\frac{\tilde{\delta}^2}{h^2}\right]\frac{\partial_x q_l \partial_x h}{h}\right.
$$
$$
+\left[-\frac{3(4h+\tilde{\delta}\varepsilon_H)}{2h} + \xi\frac{\tilde{\delta}^2}{h^2}\right]\frac{q_l}{h}\partial_{xx}h + \frac{1}{2}\left[9 + \frac{3\tilde{\delta}\varepsilon_H}{h} - \frac{\xi\tilde{\delta}^2}{h^2}\right]\partial_{xx}q_l
$$
$$
+\left.\frac{\xi}{3}\frac{\tilde{\delta}^2\varepsilon_H}{Da}\partial_{xx}q_p\right\}. \tag{44b}
$$

From (44b), we can expect an efficient diffusion of the flow rate in the porous medium in the case of a strong cross-stream dimensionless permeability ξ/Da. One limit is then worthy of interest: $q_p \to cst$ which may be achieved when $\xi/Da \gg 1$, which gives

$$
\partial_t q_l = -\frac{17}{7}\frac{q_l}{h}\partial_x q_l + \frac{9}{7}\frac{q_l^2}{h^2}\partial_x h + \frac{1}{Fr^2}\left[\frac{5h}{6}b(h) - \frac{5(1-\tilde{\delta})^2}{4h^2}q_l\right]
$$
$$
+\frac{1}{Re}\left\{4\frac{q_l(\partial_x h)^2}{h^2} - \frac{9}{2}\frac{\partial_x q_l \partial_x h}{h} - 6\frac{q_l}{h}\partial_{xx}h + \frac{9}{2}\partial_{xx}q_l\right\}, \tag{45}
$$

which corresponds to a liquid film flow on a impermeable solid wall at $y = \tilde{\delta} = \delta - \delta_B$ with a no-slip boundary condition. The approximate momentum balance (45) can also be derived from (44a) for isotropic or moderately anisotropic porous media ($\xi = O(1)$) in the limit $q_p \ll 1$, which is achieved at very low permeabilities ($Da \to 0$). [1] observed a convergence of the solutions of their two-equation model, i.e. (27, 40) with $\xi = 1$, to the solutions of (43, 45) at low values of the porous medium thickness ($\delta = 0.1$) for which q_p is small.

In the remainder of this paper, we discuss and compare the solutions to the three-equation models (27, 35), and (43, 44), and to the two-equation models (27, 40), and (43, 45). For convenience, these models are referred to as three-equation full and approximate models, and two-equation full and no-slip models respectively.

4.4 Linear Stability Analysis

We next turn to the stability analysis of the flat film solution based on the three-equation full and approximate models (27, 35) and (43, 44), and the two-equation extension of Samanta's model (27, 40). We compare our results to the solutions of the Orr-Sommerfeld equations (13a) in an attempt to validate our modelling approach. Figure 12 presents the marginal stability curves for the three-equation models. As for the Orr-Sommerfeld analysis presented in figure 4, a dual role of anisotropy on the stability of the film is observed depending on the value of the Darcy number. However, at low values of Re, the models predict a decrease of the range of unstable wavenumbers as ξ is raised, which is not observed with the Orr-Sommerfeld analysis. This effect is weak in the case of the full model (cf. panel b) but noticeable in the case of the approximate model (panel d).

Figure 13 compares the spatial growth rates and marginal stability curves of the three and two-equation models to the Orr-Sommerfeld analysis in the limit of low cross-stream permeability ($\xi = 1000$). If the three-equation model satisfactorily reproduces the Orr-Sommerfeld analysis, the two-equation full model does not. This inadequacy is a consequence of the ansatz (37) which yields an overestimation of the contribution of the cross-stream permeability on the viscous diffusion of the waves (coefficients $\tilde{L}(1)$ and $\tilde{M}(1)$).

(a) $Da = 0.001$

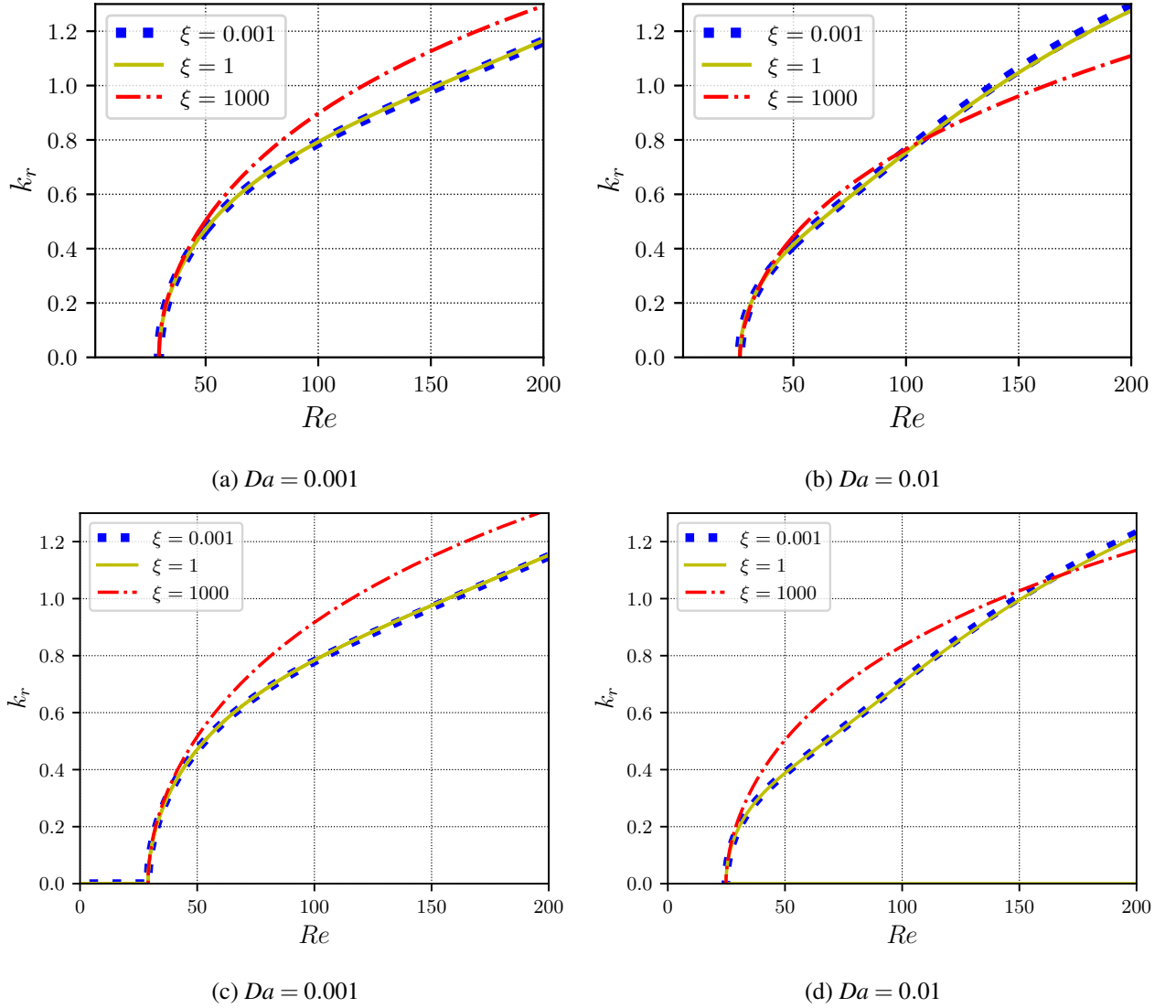(b) $Da = 0.01$

(c) $Da = 0.001$

(d) $Da = 0.01$

Figure 12: (a), (b) Marginal stability curves corresponding to the three-equation full model (27, 35) (c), (d) marginal stability curves corresponding to the three-equation approximate model (43, 44) for different permeabilities and different anisotropy parameters. All the curves are plotted when $\varepsilon_H = 0.78$, $\delta = 0.5$, $\Delta = 0.001$, $\theta = 4.6°$ and $Ka = 769.8$. Compare to the O.S. analysis in figure 4.

(a) Da = 0.01

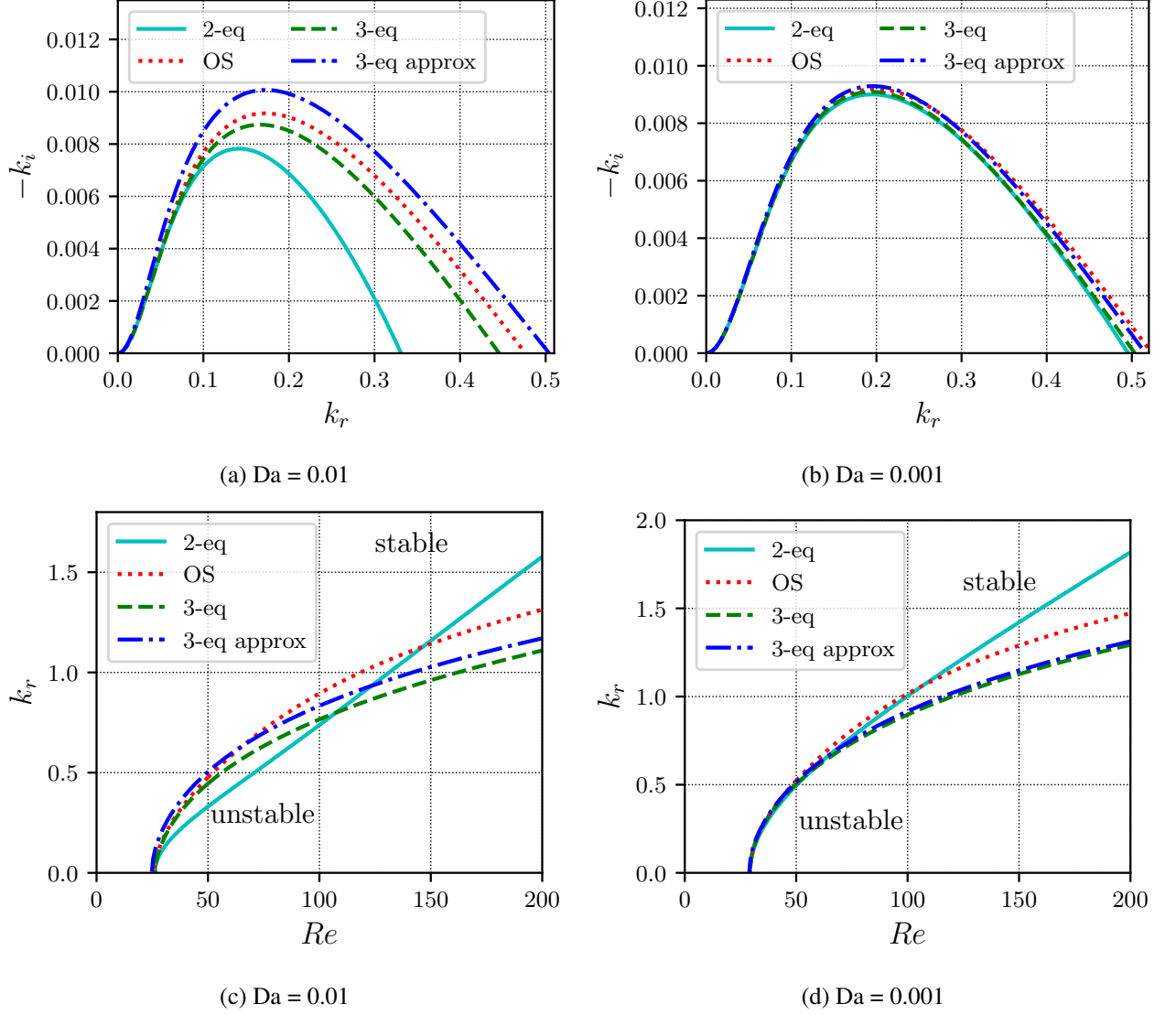(b) Da = 0.001

(c) Da = 0.01

(d) Da = 0.001

Figure 13: Comparisons of the marginal stability curves for the two-equation full (27,40), three-equation full (27, 35), and approximate model (43, 44) with the Orr-Sommerfeld analysis, (a), (b) spatial growth-rate for $Re = 50$; (c), (d) marginal stability curves. All the curves are plotted with the parameter set $\xi = 1000$, $\varepsilon_H = 0.78$, $\delta = 0.5$, $\Delta = 0.001$, and $Ka = 769.8$ and $\theta = 4.6°$.

We conclude that the three-equation models offer reliable alternatives to the Orr-Sommerfeld analysis and are quite accurate. In the isotropic case ($\xi = 1$) and relatively large permeability ($Da = 0.01$), the three-equation approximate model is less accurate than the full model, predicting reduced intervals of unstable wavenumbers than the full model and Orr-Sommerfeld analysis. However, this is expected as the polynomial approximation leading to the approximate model assumes that the base-flow velocity profile presents a constant velocity distribution in the bulk of the porous layer (Darcy region). Such a Darcy region is already not observed at $Da = 0.01$ (cf. figure 2).

5 Nonlinear travelling wave solutions

We next turn to the construction of the nonlinear travelling wave (TW) solutions to the models. These solutions correspond to waves propagating at a constant speed and with a constant shape. The variables are then functions of the coordinate $\zeta = x - ct$ in the moving frame at speed c of the wave. The system of equations then reduces to a set of ordinary differential equations, which are recast into an autonomous dynamical system. The first step is the integration of the mass balance (27) with respect to ζ, which gives $q = q_l + q_p = cH + q_0$ where $q_0 = \int_0^H (u - c) \, dy$ is the constant flow rate in the moving frame of the wave. Substitution of $cH + q_0$ for q then leads to

$$\frac{d\boldsymbol{U}}{d\zeta} = F(\boldsymbol{U}, c), \tag{46}$$

where U is a three-dimensional vector $(H, H', H'')^t$ for the two-equation models (27, 40), and (43, 45), and a four-dimensional vector $(H, H', H'', q_p)^t$ for the three-equation models (27, 35), and (43, 44), the primes denoting derivatives with respect to ζ. The locations of the fixed-point solutions to (46) verify

$$H^3 \left\{ I^{(l)}(H) + I^{(p)}(H) \right\} - cH - q_0 = 0, \tag{47}$$

which admits three solutions, of which only two may be positive. Consequently, a maximum of two fixed points is observed in the phase space for any value of the phase speed c.

The moving-frame flow rate q_0 is determined by imposing either an integral constraint or the location of one fixed point, which corresponds to selecting the thickness of the uniform film, i.e. $q_0 = I^{(l)}(1) + I^{(p)}(1) - c$ for a uniform-film thickness equal to unity. Two integral constraints are useful and physically relevant. The first one is to fix the averaged thickness of the film, i.e. $\langle H \rangle \equiv \lambda^{-1} \int_0^\lambda H \, d\zeta = 1$, which corresponds to the conservation of mass in a time-dependent simulation with periodic boundary conditions (λ denoting the period). This condition is referred to hereinafter as the constant-thickness formulation. The second useful constraint, or constant-flux formulation, consists in $\langle q \rangle = I^{(l)}(1) + I^{(p)}(1)$, which corresponds to the conservation of mass in a time-dependent simulation with open-domain boundary-conditions at the outlet and a periodic forcing at the inlet [33].

The autonomous dynamical system (46) constitutes an integral boundary value problem whose eigenvalue is the phase speed c of the waves. Branches of solutions are constructed by varying c, which is the principal continuation parameter of the computations. More specifically, TW solutions are obtained starting from the fixed-point solution corresponding to a flat film, i.e. $H = 1$ and $q_p = I^{(p)}(1)$. A limit cycle emerges from the fixed point through a Hopf bifurcation occurring at the marginal stability conditions ($k_i = c_i = 0$) predicted by the linear stability analysis. Solitary waves are next obtained as a result of a homoclinic bifurcation by increasing the period λ of the limit cycles to large values up to the point at which they collide to the second fixed point.

Figures 14 and 15 present limit cycles of large extensions ($\lambda = 200$) which approach homoclinicity for the constant-thickness formulation ($\langle H \rangle = 1$) at $Da = 0.001$ and $Da = 0.01$, respectively. Since truly solitary waves of infinite period cannot be numerically obtained, we refer to these waves as solitary waves. These waves present a slowly varying tail corresponding to the one-dimensional unstable manifold of the fixed point, and capillary ripples at its front, related to the two (or three)-dimensional stable manifold of the saddle-focus fixed point in the phase space. We compared the solutions to the three-equation full model (27, 35), and approximate

(a) $Da = 0.001$, $\xi = 1$

(b) $Da = 0.001$, $\xi = 1$

(c) $Da = 0.001$, $\xi = 1000$
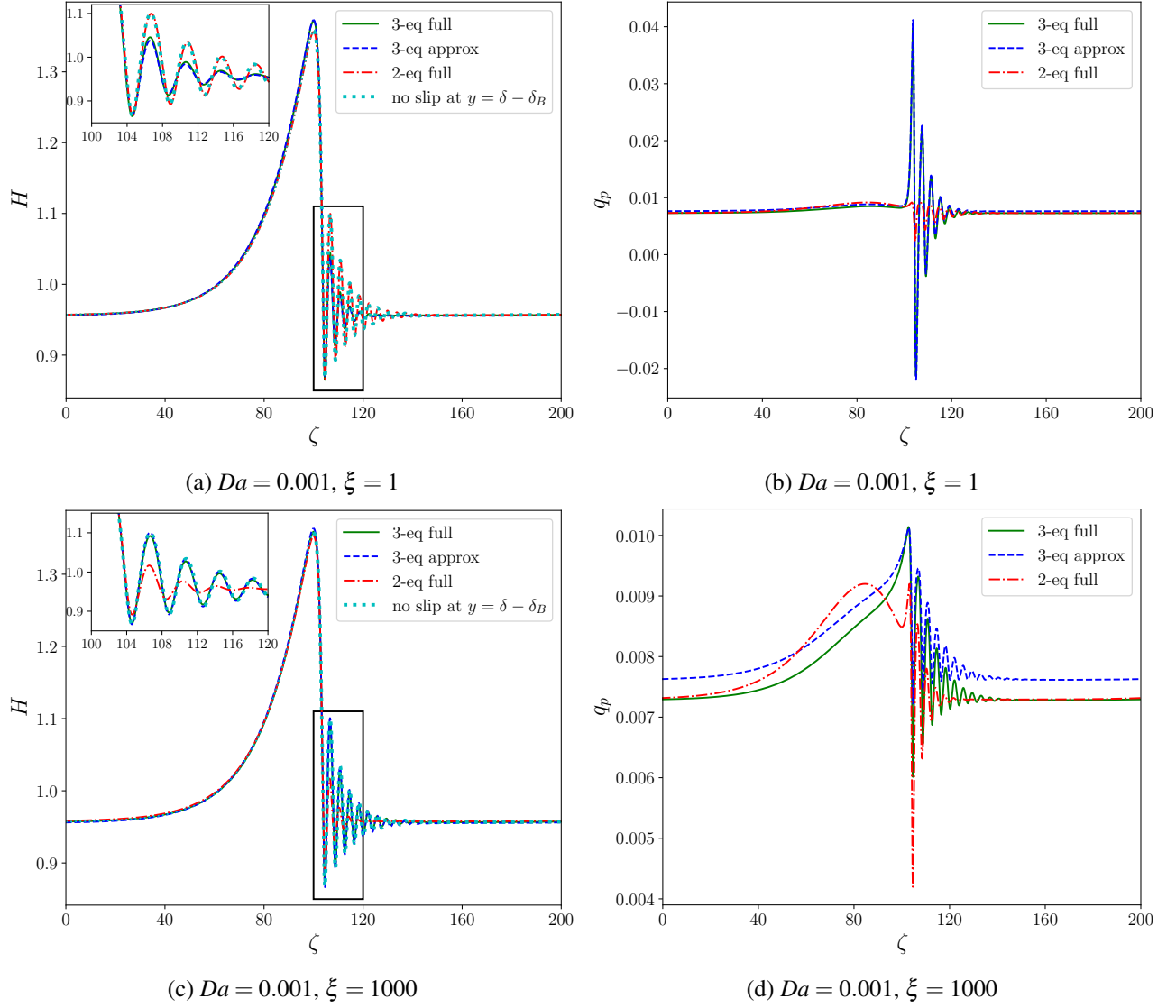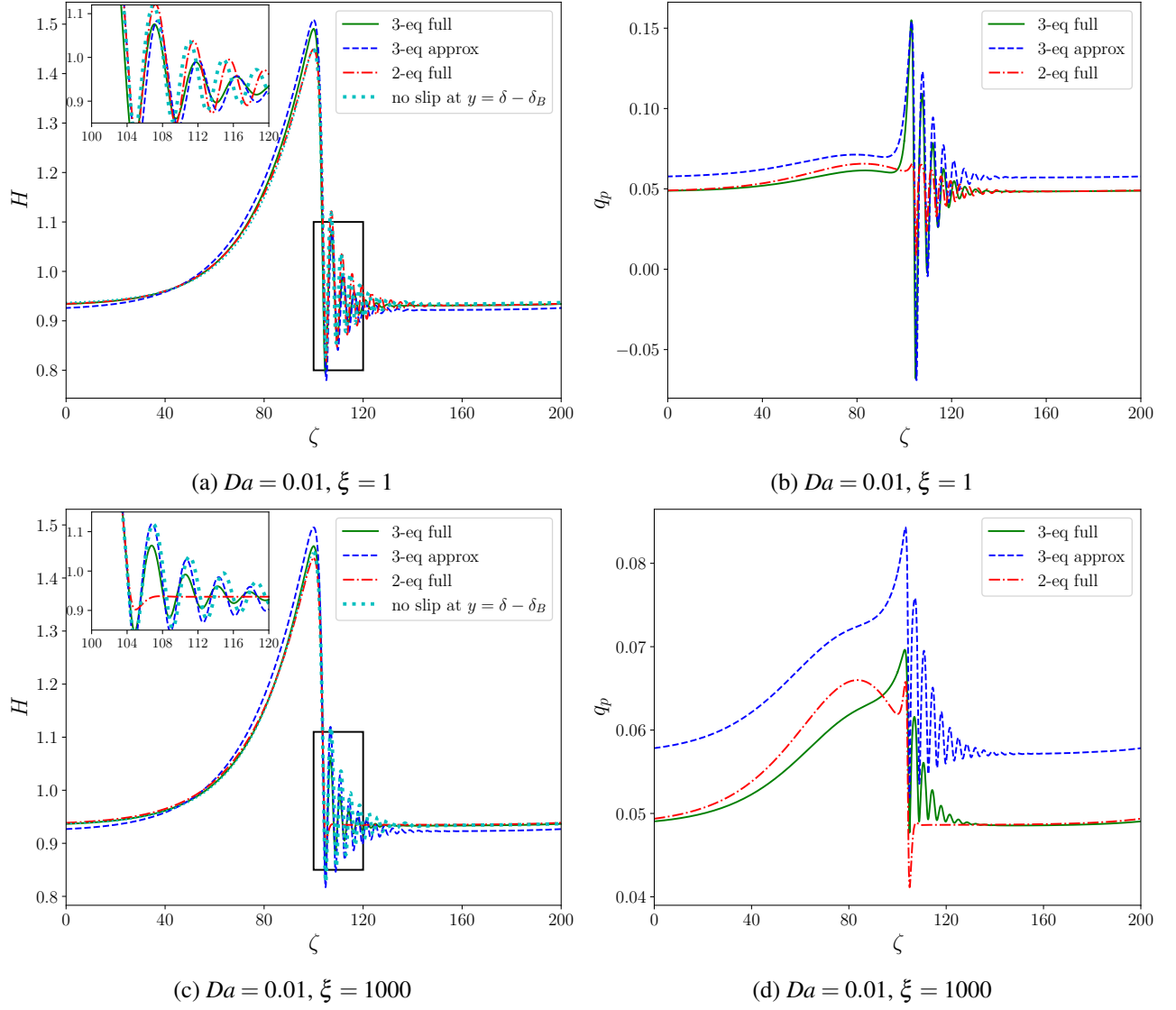
(d) $Da = 0.001$, $\xi = 1000$

Figure 14: Non-linear travelling waves for the two-equation full (27, 40), three-equation full (27, 35), approximate (43, 44) models, and for the no-slip model (43,45) (impermeable wall at $y = \delta - \delta_B$), when $Da = 0.001$, $\varepsilon_H = 0.78$, $\delta = 0.5$, $\Delta = 0.001$, $Ka = 769.8$, $\theta = 4.6°$, and $\lambda = 200$. H indicates the thickness of the entire layer (porous and liquid).

(a) $Da = 0.01$, $\xi = 1$

(b) $Da = 0.01$, $\xi = 1$

(c) $Da = 0.01$, $\xi = 1000$

(d) $Da = 0.01$, $\xi = 1000$

Figure 15: Idem figure 14 except for $Da = 0.01$.

model (43, 44), and to the two-equation full model (27, 40), and no-slip model (43, 45). For a small value of the Darcy number ($Da = 0.001$), a remarkable agreement is achieved between the solutions of the full and approximate three-equation models as the polynomial approximations for the velocity profiles employed in subsection §4.3 hold in the limit $Da \ll 1$. As the Darcy number is raised to $Da = 0.01$, some departures of the solutions from the approximate model to the full model are noticeable. However, the approximate model remains a convincing substitute for the full model.

In the case of an isotropic porous medium ($\xi = 1$), the wave profiles obtained with the two-equation full model and the no-slip model nearly collapse on single curves for the two tested values of the Darcy number. This agreement can be comprehended by computing the flow rate in the porous medium $\tilde{q}_p = q \int_0^H I d_p f(y; H) \, dy$ corresponding to the single velocity profile ansatz (37). As can be observed from panels b in figure 14 and 15, $\tilde{q}_p$ presents moderate fluctuations so that $\tilde{q}_p$ can be assumed somewhat constant. Since $q_p = cst$ or $q_p \ll 1$ are the conditions yielding the no-slip model, this explains the observed concordance of results from the no-slip and two-equation full model at $\xi = 1$. At $\xi = 1000$, solitary-wave solutions to the two-equation full model present capillary ripples whose number and amplitude are significantly lower than with the other models, to the point that for $Da = 0.01$, only one capillary ripple is observable at the front of the wave (see figure 15c). This discrepancy results from the overestimation of the contributions of the porous medium to the viscous diffusion terms in the momentum balance (40) implied by the one-velocity ansatz (37).

A comparison of the solutions of the three-equation models at $\xi = 1$ and $\xi = 1000$ shows that the fluctuations of the flow rate q_p in the porous medium are efficiently attenuated by lowering the cross-stream permeability (thus raising ξ). This explains the convergence of the solutions to the three-equation and no-slip models at $\xi = 1000$. Interestingly, lowering the cross-stream permeability enhances the amplitude of the capillary ripples. We anticipate that this enhancement results from the attenuation of the mass exchange at the liquid-porous interface as ξ is raised. Finally, let us note that the intensity of the mass exchange between the porous and liquid regions, as reflected by the fluctuations of q_p, is predicted to be much higher with the three-equation models than with the two-equation full model in the isotropic case ($\xi = 1$). This suggests that the assumption of a complete slaving of the velocity distribution in the porous medium to the one in the liquid medium, i.e. ansatz (37), as employed by [1], may be too restrictive.

6 Time-dependent simulations

In this section, we present some time-dependent numerical simulations of the three-equation and two-equation full models (27, 35) with periodic boundary conditions (closed flow), and with outlet open boundary conditions and forcing at the inlet (open flow). Computations have been performed using finite differences and the method of lines, which can be easily employed in the case of evolution equations [34], for which the system of partial differential equations can be written as

$$\mathbf{U}_t = F(\mathbf{U}, \mathbf{U}_x, \mathbf{U}_{xx}, \ldots), \tag{48}$$

where the indices refer to temporal or spatial derivatives. $\mathbf{U}$ is the vector that contains the unknowns (in this particular case h, q and q_p). The spatial derivatives of our system (48) are first discretized and replaced by algebraic approximations using second-order central finite differences. As a consequence, (48) is transformed into an initial value problem for the vector $\tilde{\mathbf{U}}$ of discrete unknowns on the chosen numerical grid.

$$\frac{d\tilde{\mathbf{U}}}{dt} = \tilde{F}(\tilde{\mathbf{U}}). \tag{49}$$

System (49) is integrated in time using a high-order Rosenbrock Wanner scheme [35]. These schemes are implicit Runge Kutta schemes optimised to reduce the numerical cost of the matrix inversions of the implicit steps. The Rosenbrock Wanner schemes allow reusing the jacobian matrix factorization across the process internal steps to avoid re-evaluation and factorization. High order time discretizations are thus enabled without the prohibitive cost of these operations.

We first consider periodic boundary conditions (closed flow) with an initial condition corresponding to a finite amplitude monochromatic disturbance as

$$H(x,0) = 1 + 0.1 \cos\left(\frac{2\pi x}{L}\right), \tag{50a}$$

$$q_i(x,0) = h(x,0)^3 \, I^{(i)}(H(x,0), \tag{50b}$$

where L is the non-dimensional length of the periodic domain. The parameter values chosen for our simulation are $\varepsilon_H = 0.78$, $\theta = 4.6°$, $\delta = 0.5$, $\Delta = 0.001$, $Ka = 769.8$, $Re = 50$, the extension of the periodic domain being set to $L = 100$. A one-humped solitary-like wave emerges rapidly from the initial growth of the sinusoidal perturbation. The wave then travels at a constant speed and shape.

Figures 16 and 17 show the profiles of the waves and the distributions of flow rate at the final stage of the computation for different Darcy numbers and anisotropy parameters. These waves belong to the branch of one-hump travelling-wave solutions that we computed in §5 with a continuation method. Comparisons (not shown) of the solutions obtained with AUTO07P and the time-dependent simulations show a remarkable agreement, which validates our numerical scheme. Figures 16 and 17 complete our discussion of the effect of anisotropy on TWs by comparing directly the high cross-stream permeability case ($\xi = 0.001$) to the low cross-stream permeability case ($\xi = 1000$). At a low value of the Darcy number, $Da = 0.001$, anisotropy does not significantly affect the shape of the waves as the flow in the porous medium is weak, and the profiles are nearly superimposed. For a higher permeability, $Da = 0.01$, raising ξ has a more noticeable effect on the wave profiles. We note that this effect is also different depending on permeability. At $Da = 0.001$, raising ξ enhances the capillary ripples, whereas these capillary waves are damped at $Da = 0.01$. At low values of ξ, the intensity of the variations of the flow rate q_p is relatively large, and thus a significant amount of mass is exchanged between the porous and liquid regions of the flow, at least in the case of a relatively permeable porous medium. Following our discussion of the linear stability in §3.4, the permeability of the liquid-porous interface promotes the stability of the film and thus should have a damping effect on the capillary ripples, which explains that by suppressing the exchange of mass between the liquid and porous region, raising ξ promotes the amplitude of the capillary ripples. However, raising ξ also enhances the diffusion of the waves as reflected by the diffusion terms $\xi \tilde{L}_l^{(l)}$ and $\xi \tilde{M}_l^{(l)}$ in (35), which has a damping effect on the short-wave capillary ripples. This effect is, however, dominant only if the flow in the porous medium is significant, therefore at relatively high values of the Darcy number.

Compared to the three-equation full model (27, 35), the two-equation model (27, 40), overestimates the damping effect of raising the anisotropic parameter ξ. This inconvenience is related to the misrepresentation of the contributions of the porous medium to the viscous diffusion which arises with a one-function ansatz (37) for the velocity field.

Finally, we present a time-dependent simulation of the three-equation full model with outlet open boundary conditions in an extended domain. This choice enables us to approach the experimental conditions of an open flow. In order to simulate the natural evolution of the film as a response to the ambient noise, we superimpose to a constant film thickness a white noise signal of weak amplitude, such that the inlet film thickness $H(x=0,t)$ fluctuates in the interval $[0.9, 1.1]$. Inlet conditions for the other fields ($q_l(x=0,t)$ and $q_p(x=0,t)$) correspond to the Nusselt solution, i.e. $(q_l(x=0,t) = H(x=0,t)^3 I^{(l)}(H(x=0,t))$. Dealing with the outlet boundary is somewhat tricky as we ideally should use a boundary that perfectly absorbs the leaving waves. However, due to the intrinsic convective nature of the studied phenomena, a more trivial boundary is considered. The oscillations induced by non-ideal outlet boundary conditions will only affect a small portion of the domain. Thence, a simple no-flux boundary is applied at the domain outlet. As for the periodic case, a semi-discrete scheme is used (following the method of lines) coupled with an implicit ODE solver. Simulation parameters are identical as previously, with a relatively permeable isotropic substrate ($Da = 0.01$ and $\xi = 1$).

Figure 18 presents a snapshot of the film evolution at the end of the simulation as well as a spatio-temporal diagram showing the wavy dynamics, which is achieved once the transient regime of the flow has been advected out of the numerical domain. The typical coarsening dynamics of falling film flows is clearly observable as
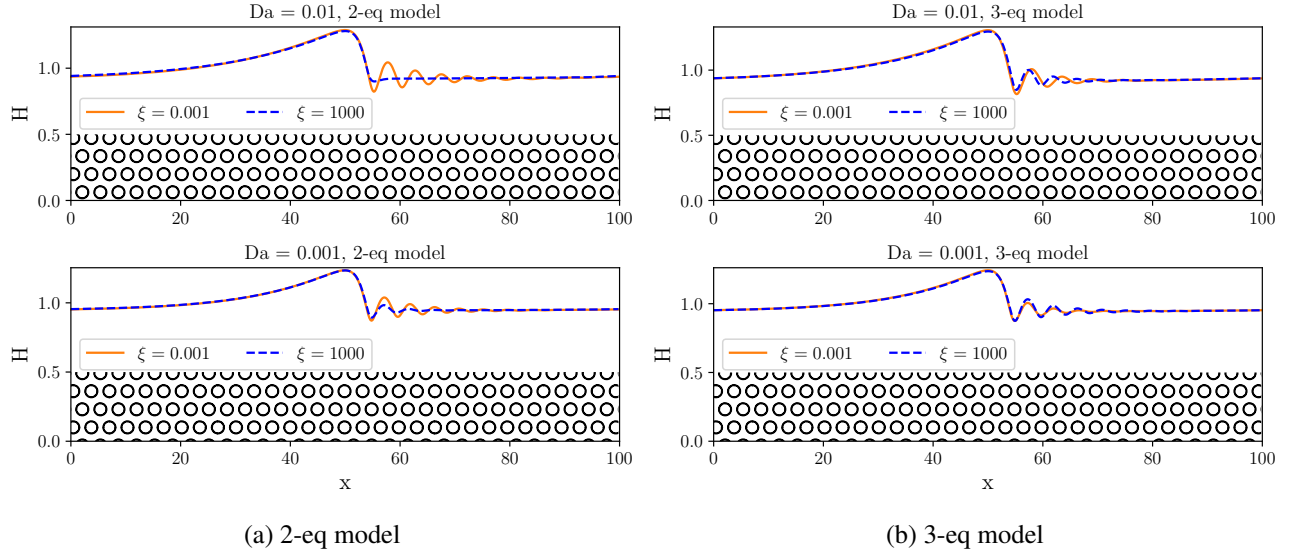
(a) 2-eq model

(b) 3-eq model

Figure 16: Snapshots of the film height at the end of time-dependent simulations with periodic boundary conditions with (a) the two-equation full model (27, 40) and (b) the three-equation full model (27, 35) for $\varepsilon_H = 0.78$, $\delta = 0.5$, $\Delta = 0.001$, $\theta = 4.6°$, $Re = 50$ and $\lambda = 100$ for different anisotropic parameters.
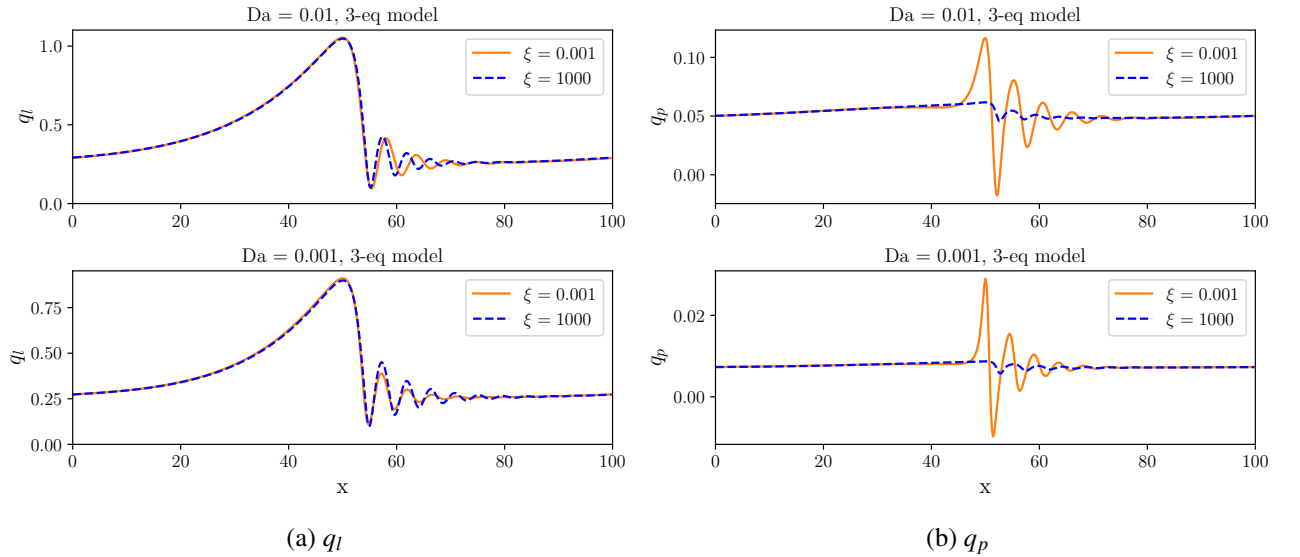

(a) q_l

(b) q_p

Figure 17: Snapshots of the flow-rate distributions at the end of time-dependent simulations with periodic boundary conditions with the three-equation full model (27, 35) ; (a) flow rate q_l in the liquid region, (b) flow rate q_p in the porous region. Identical set of parameters to figure 16.
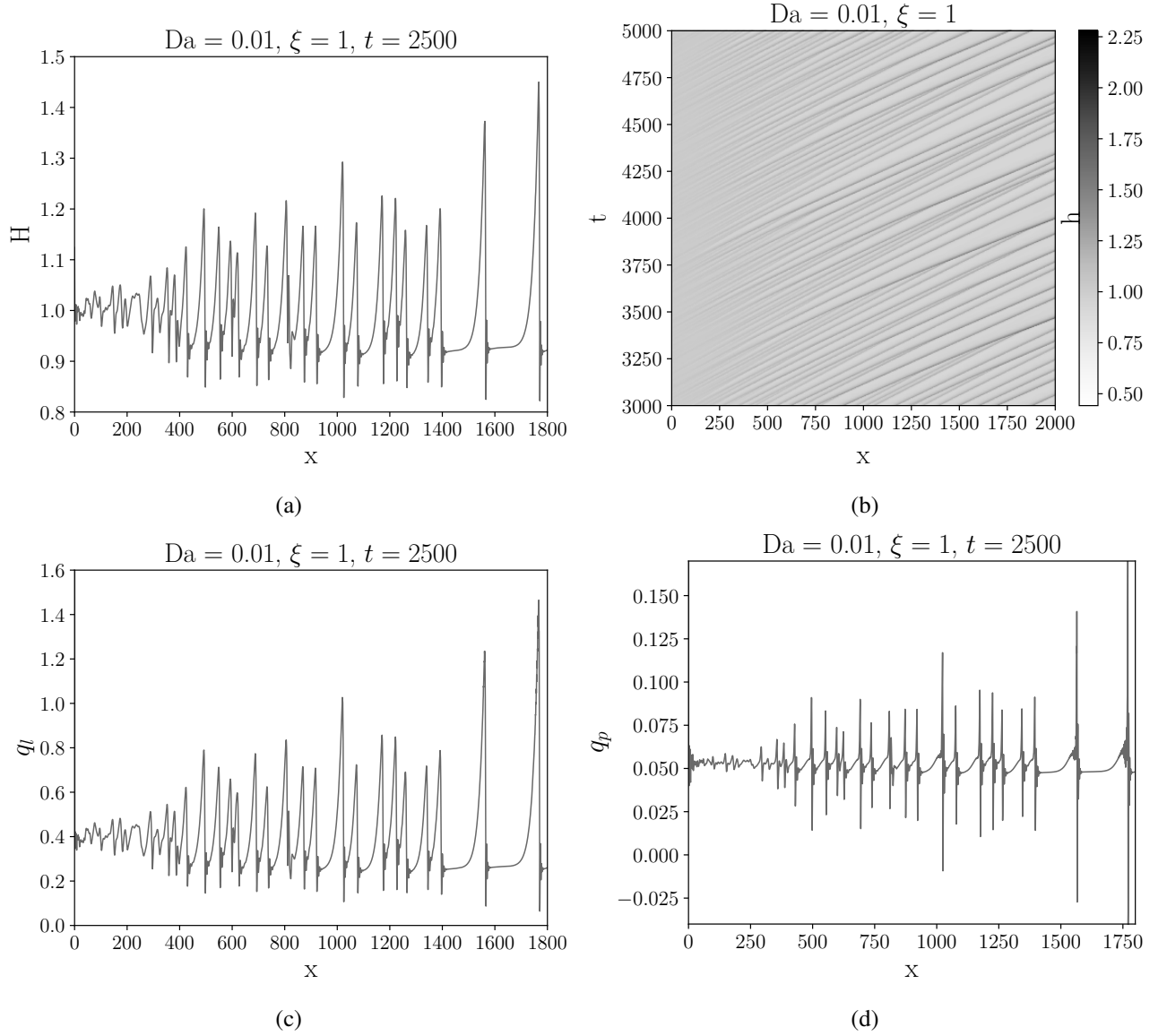
Figure 18: Simulation of the response of the film to a noise at inlet. The simulation is based on the three-equation full model (27, 35). Panels a, b and c are snapshots of the free surface elevation and flow rates in the liquid and porous region at the end of the simulation. Panel b is a spatio-temporal diagram. Light (dark) regions correspond to small (large) elevations. Parameters are $Da = 0.01$, $\varepsilon_H = 0.78$, $\delta = 0.5$, $\Delta = 0.001$, and $Ka = 769.8$, $\theta = 4.6°$ and $\xi = 1$ (isotropic porous medium).

large-amplitude waves travel faster and capture the waves which precede them. The downstream dynamics of the flow is then organised by solitary waves in interaction [6]. Interestingly, the flow rate q_p in the porous medium may rise to quite large values under the large-amplitude solitary waves, corresponding to roughly three times its value for the Nusselt uniform-film solution. We thus conclude that the wavy dynamics of the film triggers a much more efficient exchange of mass between the porous and liquid media than anticipated from the work of [1] where the velocity in the porous medium was assumed to closely follow the velocity distribution in the liquid layer as implied by the ansatz (37).

7   Summary and conclusions

The effects of anisotropy on the stability and nonlinear evolution of a falling film on an inclined plane have been investigated in the framework of both a one-domain composite description of the entire liquid and porous domains introduced by [16] and the two-domain approach proposed by [15]. We have extended the weighted-residual modelling approach followed by [1] by decoupling the flows in the porous and liquid regions. The result is the three-equation semi-analytical model (27, 35) whose coefficients have been tabulated numerically. In the limit $Da \ll 1$, we have shown that this model can be simplified into (43, 44) using polynomial approximations of the velocity profile.

Orr-Sommerfeld stability analysis of the base flow has been conducted with either the one-domain and two-domain formulations, showing a good agreement between the two. Anisotropy does not affect the threshold of linear instability. However, a non-trivial dual effect of anisotropy on the film stability is observed depending on the permeability of the porous medium. Following the conclusions of [1] in the isotropic case, we expected the linear stability of the film on the porous substrate to be nearly equivalent to the stability of a film on an impermeable no-slip effective boundary located at $y = \delta - \delta_B$ (no-slip model). However, our results show that this equivalence is observed only for relatively thin porous substrates (cf. figure 11). For a thicker porous layer, our computations show a weak amplification of the instability at the threshold at large permeabilities and an attenuation otherwise, as compared to the effective no-slip model proposed by [1]. This slight discrepancy on the instability threshold likely results from the significant differences observed for the velocity profiles in the porous region at large permeabilities (see figure 2). We anticipate that the significant attenuation of the instability further from the threshold as compared to the no-slip model should result from the exchange of mass at the porous-liquid interface, which is allowed by the permeability of the porous substrate. Whatever the reason, it is clear that the porous substrate plays a more important role in the stability of the film than we anticipated.

Our study of nonlinear waves has been based on the weighted residual three-equation models that we derived to account for the decoupling of the flows in the porous and liquid regions. This approach has been validated in the linear regime by comparison with the Orr-Sommerfeld analysis. We have constructed travelling-wave (TW) solutions by a continuation method and performed time-dependent simulations with both periodic boundary conditions (closed flow) and open boundary conditions at the outlet (open flow). The emergence of TW solutions out of the time-dependent simulations for periodic boundary conditions enabled us to validate our numerical scheme by comparisons with the solutions to the dynamical system. TW solutions are close to the corresponding ones for the no-slip model (effective impermeable boundary at $y = \delta - \delta_B$) at low permeabilities. However, for the isotropic case $\xi = 1$, the intensity of the fluctuations of the flow rate q_p in the porous medium, and therefore the exchange of mass at the liquid-porous interface, is significant and impact the amplitude of the capillary ripples. Raising ξ attenuates the fluctuations of q_p, thus limiting the mass exchange at the liquid-porous interface. This mechanism amplifies the capillary ripples at low values of Da. However, damping of the capillary ripples is instead observed at larger values of Da when ξ is raised. This is explained by the increased efficiency of the viscous diffusion of the waves as the intensity of the flow in the porous layer is raised along with the permeability.

Finally, our time-dependent simulations of a noise-driven wavy film show that the fluctuations of the flow rate in the porous medium can be large due to the onset of very large-amplitude solitary waves that dominate the dynamics of the film. We conclude that the influence of the flow in the porous layer on the film dynamics

is much stronger than admitted in previous studies. The approximate three-equation model (43, 44) offers a reliable alternative to the more complex semi-analytical model (27, 35) for a large range of *Da* numbers, and thus constitutes an interesting tool for later works.

Declaration of Interests: The authors report no conflict of interest.

Acknowledgements

A Coefficients of the weighted residual model

The coefficients of the three-equation full model (27), (35) involve $f_i(y;H)$ and their derivatives with respect to H, $g_i = \partial_H f_i$, $a_i = \partial_{HH} f_i$ which verify

$$L g_i = -C'_{ij} Id_j, \quad g_i|_{y=0} = 0, \quad \text{and} \quad \partial_y g_i|_{y=H} = C_{il}, \quad \int_0^H Id_j g_i = -\delta_{jl} f_i(H;H), \tag{51a}$$

and

$$L a_i = -C''_{ij} Id_j, \quad a_i|_{y=0} = 0, \quad \text{and} \quad \partial_y a_i|_{y=H} = 2C'_{il}, \quad \int_0^H Id_j a_i = -2\delta_{jl} g_i(H;H), \tag{51b}$$

where $C'_{ij} = dC_{ij}/dH$ and $C''_{ij} = d^2 C_{ij}/dH^2$. The computation also involves the following functions

$$l_i = \int_0^y f_i \, dy, \quad m_i = \int_0^y g_i \, dy, \quad b_i = \int_0^y a_i \, dy, \tag{51c}$$

$$n_i = \int_H^y \frac{\partial_y f_i}{\varepsilon} \, dy, \quad o_i = \int_H^y \frac{\partial_y g_i}{\varepsilon} \, dy, \quad \beta_i = \int_H^y \frac{\partial_y a_i}{\varepsilon} \, dy, \tag{51d}$$

$$r_i = \int_H^y \frac{l_i}{\kappa_x} \, dy, \quad s_i = \int_H^y \frac{m_i}{\kappa_x} \, dy, \quad \alpha_i = \int_H^y \frac{b_i}{\kappa_x} \, dy. \tag{51e}$$

The expressions of the 54 coefficients are then given below:

$$S_i^{(k)} = \frac{1}{H^2} \int_0^H f_i w_k \, dy, \tag{52a}$$

$$F_{ij}^{(k)} = \frac{1}{H} \int_0^H \varepsilon^{-2} \left[\partial_y \varepsilon f_j l_i + (f_i f_j - \partial_y f_j l_i)\varepsilon - g_i \varepsilon^2 \right] w_k \, dy, \tag{52b}$$

$$G_{ij}^{(k)} = \int_0^H \varepsilon^{-2} \left[-\partial_y \varepsilon f_i m_j - \varepsilon(f_i g_j - \partial_y f_i m_j) \right] w_k \, dy, \tag{52c}$$

$$J_i^{(k)} = 2g_i|_H w_k|_H + (2a_i|_H + C_{il}) \Upsilon_k + \int_0^H (a_i + \beta_i \varepsilon) w_k \, dy, \tag{52d}$$

$$\tilde{J}_i^{(k)} = \int_0^H -\alpha_i \varepsilon w_k \, dy, \tag{52e}$$

$$K_i^{(k)} = -2\frac{1}{H} \left\{ f_i|_H w_k|_H + 2g_i|_H \Upsilon_k + \int_0^H (g_i + o_i \varepsilon) w_k \, dy \right\}, \tag{52f}$$

$$\tilde{K}_i^{(k)} = \frac{2}{H} \int_0^H s_i \varepsilon w_k \, dy, \tag{52g}$$

$$L_i^{(k)} = \frac{1}{H} \left\{ (f_i|_H w_k|_H - 2g_i|_H \Upsilon_k) - \int_0^H (g_i + o_i \varepsilon) w_k \, dy \right\}, \tag{52h}$$

$$\tilde{L}_i^{(k)} = \frac{1}{H} \int_0^H s_i \varepsilon w_k \, dy, \tag{52i}$$

$$M_i^{(k)} = \frac{1}{H^2} \left\{ 2f_i|_H \Upsilon_k + w_k|_H + \int_0^H (f_i + n_i \varepsilon) w_k \, dy \right\}, \tag{52j}$$

$$\tilde{M}_i^{(k)} = -\frac{1}{H^2} \left\{ \int_0^H r_i \varepsilon w_k \, dy \right\}, \tag{52k}$$

$$\Upsilon_k = \int_0^H \varepsilon w_k \, dy, \tag{52l}$$

$$I^{(k)} = \Upsilon_k / H^3. \tag{52m}$$

These expressions must be contrasted with the corresponding ones for the two-equation model obtained by [1], who chose the one-function ansatz (37). We have carefully checked that, setting ξ to one and dropping the indices and suffices in (52) yields the correct expressions for Samanta's model. However, they are written differently than in [1] due to a different —yet equivalent— choice (38) for the definition of the test function f.

We note that the base flow U_B verifies

$$U_B = H^3 \left[I^{(l)}(H) f_l(y; H) + I^{(p)}(H) f_p(y; H) \right]. \tag{52n}$$

Since the reference scale for the velocity is the free-surface velocity of the base flow for the reference thickness $H = 1$, we have the relation

$$1 = I^{(l)}(1) f_l(1; 1) + I^{(p)}(1) f_p(1; 1). \tag{52o}$$

The linear stability analysis of the stationary solutions to the system (27) and (35) requires to compute the variations with respect to H of the weights, which verify

$$L\partial_H w_i = 0, \quad \partial_H w_i|_{y=0} = 0, \quad \text{and} \quad \partial_{yH} w_i|_{y=H} = \delta_{il} \frac{Re}{Fr^2}, \tag{52p}$$

so that $\partial_H w_p = 0$. We thus have

$$\frac{d(H^3 I^{(l)})}{dH} = w_l|_H + \int_0^H \varepsilon \partial_H w_l \, dy, \quad \frac{d(H^3 I^{(p)})}{dH} = w_p|_H. \tag{52q}$$

34

B Approximation of the coefficients of the weighted residual model

We provide below the approximate expressions of the coefficients (52) corresponding to the polynomial estimate of the velocity profile.

$$
\begin{aligned}
S_l^{(l)} &\approx \frac{4(H-\tilde{\delta})^2}{5(1-\tilde{\delta})^2H^2} + O(\delta_B^2), \quad S_p^{(l)} \approx -\frac{2(H-\tilde{\delta})^3}{15(1-\tilde{\delta})^2\tilde{\delta}H^2} + O(\delta_B), \\
F_{ll}^{(l)} &\approx \frac{68(H-\tilde{\delta})}{35(1-\tilde{\delta})^2H} + O(\delta_B^2), F_{lp}^{(l)} \approx -\frac{12(H-\tilde{\delta})^2}{35(1-\tilde{\delta})^2\tilde{\delta}H} + O(\delta_B), \\
F_{pl}^{(l)} &\approx \frac{2(H-\tilde{\delta})(13\tilde{\delta}-6H)}{35(1-\tilde{\delta})^2\tilde{\delta}H} + O(\delta_B), \quad F_{pp}^{(l)} \approx \frac{(H-\tilde{\delta})^2(227\tilde{\delta}+88H)}{420(1-\tilde{\delta})^2\tilde{\delta}^2H} + O(\delta_B), \\
G_{ll}^{(l)} &\approx \frac{36}{35(1-\tilde{\delta})^2} + O(\delta_B^2), \quad G_{pp}^{(l)} \approx -\frac{4(H-\tilde{\delta})^2}{35(1-\tilde{\delta})^2\tilde{\delta}^2} + O(\delta_B), \\
G_{lp}^{(l)} &= G_{pl}^{(l} \approx -\frac{1}{2}\left[\frac{4(H-\tilde{\delta})}{35(1-\tilde{\delta})^2\tilde{\delta}}\right] + O(\delta_B), \quad J_l^{(l)} \approx \frac{16}{5(1-\tilde{\delta})^2} + O(\delta_B^2), \\
J_p^{(l)} &\approx \frac{2(H-\tilde{\delta})}{5(1-\tilde{\delta})^2\tilde{\delta}} + O(\delta_B), \quad \tilde{J}_l^{(l)} \approx \tilde{J}_p^{(l)} = O(\delta_B^3), \quad K_l^{(l)} \approx \frac{18(H-\tilde{\delta})}{5(1-\tilde{\delta})^2H} + O(\delta_B^2), \\
K_p^{(l)} &\approx -\frac{2(H-\tilde{\delta})^2}{(1-\tilde{\delta})^2\tilde{\delta}H} + O(\delta_B), \quad \tilde{K}_l^{(l)} \approx \tilde{K}_p^{(l)} \approx O(\delta_B^3), \quad L_l^{(l)} \approx \frac{24(H-\tilde{\delta})}{5(1-\tilde{\delta})^2H} + O(\delta_B^2), \\
L_p^{(l)} &\approx -\frac{6(H-\tilde{\delta})^2}{5(1-\tilde{\delta})^2\tilde{\delta}H} + O(\delta_B), \quad \tilde{L}_l^{(l)} \approx \tilde{L}_p^{(l)} \approx O(\delta_B^3), \quad M_l^{(l)} \approx \frac{18(H-\tilde{\delta})^2}{5(1-\tilde{\delta})^2H^2} + O(\delta_B^2), \\
M_p^{(l)} &\approx \frac{(8\tilde{\delta}-3H)(H-\tilde{\delta})^2}{5(1-\tilde{\delta})^2\tilde{\delta}H^2} + O(\delta_B), \quad \tilde{M}_l^{(l)} = O(\delta_B^3), \quad \tilde{M}_p^{(l)} = \frac{\delta_B(H-\tilde{\delta})}{3H^2(1-\tilde{\delta})^2} + O(\delta_B^2), \\
I^{(l)} &\approx \frac{2(H-\tilde{\delta})^3}{3(1-\tilde{\delta})^2H^3 + O(\delta_B^2)}, \quad \frac{Re}{Fr^2} \approx \frac{2}{(1-\tilde{\delta})^2} + O(\delta_B^2),
\end{aligned}
\tag{53a}
$$

$$
\begin{aligned}
S_l^{(p)} &\approx \frac{2\delta_B^2}{(1-\tilde{\delta})^2 H^2} + O(\delta_B^4), \quad S_p^{(p)} \approx \frac{2\delta_B^2}{(1-\tilde{\delta})^2 H^2} + O(\delta_B^3), \quad F_{ll}^{(p)} \approx \frac{24\delta_B^2}{5(1-\tilde{\delta})^2(H-\delta)H} + O(\delta_B^4), \\
F_{lp}^{(p)} &\approx F_{pl}^{(p)} \approx -\frac{4\delta_B^2}{5(1-\tilde{\delta})^2\tilde{\delta}H} + O(\delta_B^3), \quad F_{pp}^{(p)} \approx \frac{\delta_B^2(10\tilde{\delta}+11\tilde{\delta}\varepsilon_H+4H\varepsilon_H)}{5(1-\tilde{\delta})^2\tilde{\delta}^2\varepsilon_H H} + O(\delta_B^3), \\
G_{ll}^{(p)} &\approx \frac{12\delta_B^2}{5(1-\tilde{\delta})^2(H-\tilde{\delta})^2} + O(\delta_B^4), \quad G_{pp}^{(p)} \approx -\frac{2\delta_B^2}{5(1-\tilde{\delta})^2\tilde{\delta}^2} + O(\delta_B^3), \quad G_{lp}^{(p)} = G_{pl}^{(p)} \approx O(\delta_B^3), \\
J_l^{(p)} &\approx \frac{6\delta_B^2[2H+\tilde{\delta}(\varepsilon_H-2)]}{(1-\tilde{\delta})^2(H-\tilde{\delta})^3} + O(\delta_B^4), \quad J_p^{(p)} \approx -\frac{6\delta_B^2\tilde{\delta}^2}{(1-\tilde{\delta})^2(H-\tilde{\delta})^4} + O(\delta_B^3), \\
\tilde{J}_l^{(p)} &\approx -\frac{6\tilde{\delta}^2\delta_B^2}{(1-\tilde{\delta})^2(H-\tilde{\delta})^4} + O(\delta_B^4), \quad \tilde{J}_p^{(p)} \approx \frac{2\delta\delta_B^2}{(1-\tilde{\delta})^2(H-\tilde{\delta})^3} + O(\delta_B^3), \\
K_l^{(p)} &\approx \frac{6\delta_B^2[2H+\tilde{\delta}(\varepsilon_H-2)]}{(1-\tilde{\delta})^2(H-\tilde{\delta})^2 H}, \quad K_p^{(p)} \approx -\frac{2\delta_B^2}{(1-\tilde{\delta})^2\tilde{\delta}H} + O(\delta_B^3), \\
\tilde{K}_l^{(p)} &\approx -\frac{4\delta_B^2\tilde{\delta}^2}{(1-\tilde{\delta})^2(H-\tilde{\delta})^3 H} + O(\delta_B^4), \quad \tilde{K}_p^{(p)} \approx \frac{2\delta_B^2\tilde{\delta}}{(1-\tilde{\delta})^2(H-\tilde{\delta})^2 H} + O(\delta_B^3), \\
L_l^{(p)} &\approx \frac{3\delta_B^2[4H+\tilde{\delta}(\varepsilon_H-4)]}{(1-\tilde{\delta})^2(H-\tilde{\delta})^2 H} + O(\delta_B^4), \quad L_p^{(p)} \approx -\frac{3\delta_B^2}{(1-\tilde{\delta})^2\tilde{\delta}H} + O(\delta_B^3), \\
\tilde{L}_l^{(p)} &\approx \frac{2\delta_B^2\tilde{\delta}^2}{(1-\delta)^2(H-\tilde{\delta})^3 H} + O(\delta_B^4), \quad \tilde{L}_p^{(p)} \approx -\frac{\delta_B^2\tilde{\delta}}{(1-\tilde{\delta})^2(H-\tilde{\delta})^2 H} + O(\delta_B^3), \\
M_l^{(p)} &\approx \frac{3\delta_B^2[3H+\tilde{\delta}(\varepsilon_H-3)]}{(1-\tilde{\delta})^2(H-\tilde{\delta})H^2} + O(\delta_B^4), \quad M_p^{(p)} \approx \frac{\delta_B^2[\tilde{\delta}(\varepsilon_H+5)-H]}{(1-\delta)^2\tilde{\delta}H^2} + O(\delta_B^3), \\
\tilde{M}_l^{(p)} &\approx -\frac{\delta_B^2\tilde{\delta}^2}{(1-\tilde{\delta})^2(H-\tilde{\delta})^2 H^2} + O(\delta_B^4), \quad \tilde{M}_p^{(p)} \approx \frac{2\tilde{\delta}^2}{3(1-\tilde{\delta})^2 H^2} + O(\delta_B^4), \\
I^{(p)} &\approx \frac{2\delta_B^2[H+\tilde{\delta}(\varepsilon_H-1)]}{(1-\tilde{\delta})^2 H^3} + O(\delta_B^4).
\end{aligned}
\tag{53b}
$$

References

[1] A. Samanta, B. Goyeau, and C. Ruyer-Quil, "A falling film on a porous medium," *Journal of Fluid Mechanics*, vol. 716, pp. 414–444, 2013.

[2] A. C. P. Silveira, G. Tanguy, I. T. Perrone, R. Jeantet, F. Ducept, A. F. de Carvalho, and P. Schuck, "Flow regime assessment in falling film evaporators using residence time distribution functions," *J. Food Engng*, vol. 160, pp. 65–76, 2015.

[3] Y. Amini, J. Karimi-Sabet, M. N. Esfahany, M. Haghshenasfard, and A. Dastbaz, "Experimental and numerical study of mass transfer efficiency in new wire gauze with high capacity structured packing," *Separation Science and Technology*, vol. 54, no. 16, pp. 2706–2717, 2019.

[4] D. P. Frisk and E. J. Davis, "The enhancement of heat transfer by waves in stratified gas-liquid flow," *Int. J. Heat Mass Transfer*, vol. 15, pp. 1537–1552, 1972.

[5] P. N. Yoshimura, T. Nosoko, and T. Nagata, "Enhancement of mass transfer into a falling laminar liquid film by two-dimensional surface waves—Some experimental observations and modeling," *Chem. Engng Sci.*, vol. 51, pp. 1231–1240, Apr. 1996.

[6] H.-C. Chang and E. A. Demekhin, *Complex Wave Dynamics on Thin Films*. No. v. 14 in Studies in Interface Science, Amsterdam ; New York: Elsevier, 2002.

[7] R. V. Craster and O. K. Matar, "Dynamics and stability of thin liquid films," *Rev. Mod. Phys.*, vol. 81, pp. 1131–1198, Aug. 2009.

[8] S. Kalliadasis, C. Ruyer-Quil, B. Scheid, and M. G. Velarde, *Falling Liquid Films*, vol. 176 of *Applied Mathematical Sciences*. London: Springer London, 2012.

[9] J. P. Pascal, "Linear stability of fluid flow down a porous inclined plane," *J. Phys. D: Appl. Phys.*, vol. 32, pp. 417–422, Jan. 1999.

[10] C.-S. Yih, "Stability of Liquid Flow down an Inclined Plane," *Physics of Fluids*, vol. 6, no. 3, p. 321, 1963.

[11] I. M. R. Sadiq and R. Usha, "Thin Newtonian film flow down a porous inclined plane: Stability analysis," *Physics of Fluids*, vol. 20, p. 022105, Feb. 2008.

[12] A. Samanta, C. Ruyer-Quil, and B. Goyeau, "A falling film down a slippery inclined plane," *Journal of Fluid Mechanics*, vol. 684, pp. 353–383, 2011.

[13] C. Ruyer-Quil and P. Manneville, "Improved modeling of flows down inclined planes," *Eur. Phys. J. B*, vol. 15, pp. 357–369, May 2000.

[14] U. Thiele, B. Goyeau, and M. G. Velarde, "Stability analysis of thin film flow along a heated porous wall," *Physics of Fluids*, vol. 21, p. 014103, Jan. 2009.

[15] J. A. Ochoa-Tapia and S. Whitaker, "Momentum transfer at the boundary between a porous medium and a homogeneous fluid—I. Theoretical development," *International Journal of Heat and Mass Transfer*, vol. 38, pp. 2635–2646, Sept. 1995.

[16] C. Beckermann, R. Viskanta, and S. Ramadhyani, "Natural convection in vertical enclosures containing simultaneously fluid and porous layers," *J. Fluid Mech.*, vol. 186, pp. 257–284, 1988.

[17] C. G. Aguilar-Madera, F. J. Valdés-Parada, B. Goyeau, and J. A. Ochoa-Tapia, "Convective heat transfer in a channel partially filled with a porous medium," *International Journal of Thermal Sciences*, vol. 50, pp. 1355–1368, Aug. 2011.

[18] H. Chen and X.-P. Wang, "A one-domain approach for modeling and simulation of free fluid over a porous medium," *Journal of Computational Physics*, vol. 259, pp. 650–671, Feb. 2014.

[19] R. Liu and Q. Liu, "Instabilities of a liquid film flowing down an inclined porous plane," *Phys. Rev. E*, vol. 80, p. 036316, Sept. 2009.

[20] G. Castinel and M. Combarnous, "Convection naturelle dans une couche poreuse anisotrope.," *Rev. Therm.*, vol. 168, pp. 937–947., 1975.

[21] J. Epherre, "Critère d'apparition de la convection naturelle dans une couche poreuse anisotrope.," *Rev. Therm.*, vol. 168, pp. 949–950, 1975.

[22] F. Chen and C. F. Chen, "Convection in superposed fluid and porous layers," *Journal of Fluid Mechanics*, vol. 234, pp. 97–119, 1992.

[23] M. S. Malashetty and M. Swamy, "The onset of convection in a binary fluid saturated anisotropic porous layer," *International Journal of Thermal Sciences*, vol. 49, pp. 867–878, June 2010.

[24] I. S. Shivakumara, J. Lee, and K. B. Chavaraddi, "Onset of surface tension driven convection in a fluid layer overlying a layer of an anisotropic porous medium," *International Journal of Heat and Mass Transfer*, vol. 54, pp. 994–1001, Jan. 2011.

[25] P. Deepu, S. Dawande, and S. Basu, "Instabilities in a fluid overlying an inclined anisotropic and inhomogeneous porous layer," *Journal of Fluid Mechanics*, vol. 762, p. R2, 2015.

[26] P. Deepu, S. Kallurkar, P. Anand, and S. Basu, "Stability of a liquid film flowing down an inclined anisotropic and inhomogeneous porous layer: An analytical description," *Journal of Fluid Mechanics*, vol. 807, pp. 135–154, 2016.

[27] G. Chattopadhyay, R. Usha, and S. Millet, "Instabilities in viscosity-stratified two-fluid channel flow over an anisotropic-inhomogeneous porous bottom," *Phys. Fluids*, vol. 31, p. 012103, Jan. 2019.

[28] S. C. Hirata, B. Goyeau, and D. Gobin, "Stability of Thermosolutal Natural Convection in Superposed Fluid and Porous Layers," *Transp Porous Med*, vol. 78, pp. 525–536, July 2009.

[29] B. Goyeau, D. Lhuillier, D. Gobin, and M. Velarde, "Momentum transport at a fluid–porous interface," *International Journal of Heat and Mass Transfer*, vol. 46, no. 21, pp. 4071–4081, 2003.

[30] E. J. Doedel, A. R. Champneys, T. F. Fairgrieve, Y. A. Kuznetsov, B. Sandstede, and X. Wang, "AUTO 97: Continuation And Bifurcation Software For Ordinary Differential Equations (with HomCont)," 2008.

[31] H. C. Brinkman, "A calculation of the viscous force exerted by a flowing fluid on a dense swarm of particles," *Appl. Sci. Res.*, vol. 1, p. 27, Dec. 1949.

[32] J. Liu, J. D. Paul, and J. P. Gollub, "Measurements of the primary instabilities of film flows," *Journal of Fluid Mechanics*, vol. 250, p. 69–101, 1993.

[33] B. Scheid, C. Ruyer-Quil, U. Thiele, O. A. Kabov, J. C. Legros, and P. Colinet, "Validity domain of the benney equation including the marangoni effect for closed and open flows," *Journal of Fluid Mechanics*, vol. 527, p. 303–335, 2005.

[34] N. Cellier and C. Ruyer-Quil, "Scikit-finite-diff, a new tool for PDE solving," *Journal of Open Source Software*, vol. 4, p. 1356, June 2019.

[35] J. Rang, "Improved traditional Rosenbrock–Wanner methods for stiff ODEs and DAEs," *Journal of Computational and Applied Mathematics*, vol. 286, pp. 128–144, Oct. 2015.